We are IntechOpen,
the world's leading publisher of
Open Access books
Built by scientists, for scientists

6,900
Open access books available

186,000
International authors and editors

200M
Downloads

Our authors are among the

154
Countries delivered to

TOP 1%
most cited scientists

12.2%
Contributors from top 500 universities

CLARIVATE ANALYTICS

BOOK CITATION INDEX

INDEXED

WEB OF SCIENCE™

Selection of our books indexed in the Book Citation Index
in Web of Science™ Core Collection (BKCI)

Interested in publishing with us?
Contact book.department@intechopen.com

Gas Source MBE Grown Wavelength Extending InGaAs Photodetectors

Yong-gang Zhang and Yi Gu

State Key Laboratory of Functional Materials for Informatics, Shanghai Institute of Microsystem and Information Technology, Chinese Academy of Sciences
China

1. Introduction

Photodetectors (PDs) responding to the light in short wave infrared (SWIR) of 1-3 μm have attracted much attention because of the unique spectral features in this band. For example, the water molecules, which are the most important component of this world, have 4 important absorption bands around 1.1, 1.4, 1.9 and 2.7 μm respectively as shown in Fig.1. (Rothman et al., 2005), between them clear transmission windows exist. The high contrast characteristics make it fascinating for the observation of our earth from the satellite to get diversified information. On the earth the spectroscopy character of numerous water containing substances as fruitage, beverage and medicament in SWIR band also arouses much interests. Besides, CO_2 also has significant spectral fingerprints in this band especially those around 1.6 and 2.1 μm. Those absorption features just located in the water windows with distinct intensities, which makes them quite suitable for CO_2 distribution mapping or monitoring from space or at ground. Furthermore, many areas including spectroscopy of characteristic absorption of gases or liquids, night and fog penetrate vision, thermophotovoltaic energy conversion, thermal imaging of high temperature objects, wind detection lidar, etc. also presume upon photodetectors in this band.

To detect the light in this band for the applications mentioned above arouses mainly two trait of concern, the sensitivity and response speed. For those applications the response frequencies in the range of tens of KHz to hundreds of MHz are common despite for special communication purpose. Among different categories of photodetectors, the thermal detectors are suffering from their inherent lower response speed and sensitivity. Therefore, the photon or quantum types of detectors should play an important role in this field. Quantum type PDs in SWIR band, which are the devices concerned in this chapter, may relate to different conformations and could be constructed using different type of materials. In this chapter a review on the material issues will appear first, then concentrated on the PDs using ternary III-V material of $In_xGa_{1-x}As$ on InP substrate grown by gas source molecular beam epitaxy (GSMBE) with different type of buffer structures and configurations. The buffer layer optimization will be emphasized and wafer growth, chip processing and device characterization will be introduced in detail.
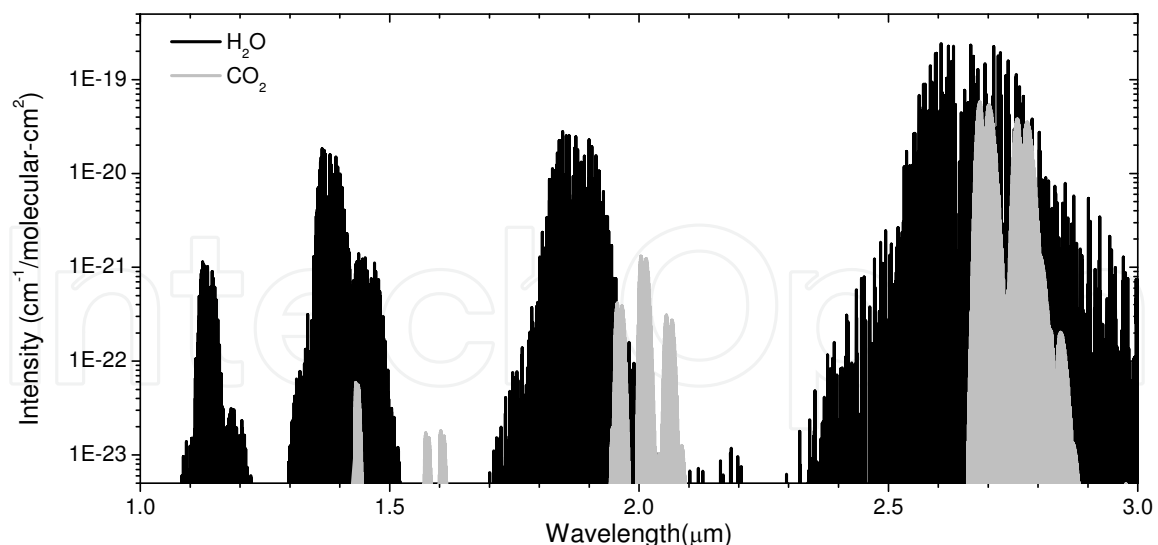
Fig. 1. Absorption characteristics of H_2O and CO_2 in short wave infrared band of 1-3 μm.

2. Material issues

2.1 Material system considerations

Quantum or photon type PDs may have different types such as photo-conductor or photovoltaic; from practical point of view photovoltaic are more preferable because the detectors can operate at zero bias with lower dark current. In SWIR band this type of detectors mainly rely on two kinds of semiconductor materials II-VI or III-V. The HgCdTe (MCT), a representative variable gap semiconductor of II-VIs, has worked successfully in SWIR band. It may be epitaxial grown on expensive but lattice matched CdZnTe substrate and excellent performances of the detectors and focal plane arrays (FPAs) have been reached. However, motivations to replace MCT especially in SWIR band always exist because of some technological problems of this material. The most important reason is the weak Hg-Te bond in MCT, which results in instabilities of the surface, interface and even the bulk material. Some other issues related to this are the difficulties in material growth and chip processing at lower temperatures with lower yield, as well as the lower operating temperature and weak radiation hardness. In III-Vs, the antimonides form some lattice matched systems covering SWIR band. The binary InAs and GaSb show nearly the same lattice constant around 6.1 Å, on those substrates different systems as quaternary InAsPSb or InGaAsSb could be grown. The quaternary InAsPSb on InAs substrate, which is the only quaternary with three group-V elements studied so far, covers the bandgap from InAs of 0.36 eV to about 0.7 eV (considering the miscibility gap) at 300K matches the SWIR perfectly. On this system liquid phase epitaxy (LPE) grown SWIR PDs have been demonstrated (e.g.: Zhang et al., 1990, 1992; Afrailov, 2010), whereas the difficulty in the control of three group-V elements As, P and Sb simultaneously to grow device quality wafers using metal-organic vapor phase epitaxy (MOVPE) or MBE remains a challenge. The other lattice matched antimonide quaternary system of InGaAsSb on GaSb, which covers the bandgap from InAs rich corner of 0.283 eV to GaSb rich corner of 0.727eV at 300K also matches the SWIR quite well. On this system LPE (e.g. Piotrowski et al., 2001), MOVPE (e.g.: Bhagwat et al., 2006) and solid source MBE (e.g.: Li et al., 1995; Liang et al., 2010) grown SWIR PDs also have been demonstrated. In this system it seems no severe limitations exist, but in practice the

difficulties in the treatment of Sb containing materials in both epitaxy and chip processing aspects still exist. For example, the compatibility of Sb source with other III-V sources in the MOVPE or MBE growth remains a problem; the wet or dry etching of certain Sb containing materials is difficult. Besides, comparing to GaAs or InP, the availability of high quality GaSb substrates at moderate price is still an issue.

In addition to MCT or antimonide materials, the III-V ternary $In_xGa_{1-x}As$ has been a good candidate to cover the SWIR band. The $In_xGa_{1-x}As$, namely the alloy of two direct bandgap binaries with direct bandgap in full region, covers the whole bandgap range of 0.36-1.43 eV of InAs and GaAs. At Indium composition x of 0.53, it is lattice matched to InP substrate with bandgap about 0.75 eV at 300K. The photodiodes using this composition with cutoff wavelength of about 1.7 μm have been sufficiently developed for decades and widely used in the optical communication wavelength of 1.31 or 1.55 μm wavelength, and their excellent performances have been definitely proved. For the ternary $In_xGa_{1-x}As$ at x from 0.53 to 1, the bandgap could be varied from 0.75 to 0.36 eV at 300K, corresponding to cutoff wavelength of 1.7 to 3.4 μm fitting the SWIR well. To shift the response to longer wavelength, the Indium content in the InGaAs alloy should be increased. For instance, to move the cutoff wavelength of the photodiodes grown on InP substrate from 1.7 μm to about 2.4 μm, the Indium contents of the InGaAs alloy have to be increased from 53% to about 80%, which introduces a quite large lattice mismatch of about +1.85% between InGaAs layer and InP substrate, in this case an extraordinary buffer layer should be inserted to prevent the degradation of the material quality. On the other hand, the full maturity of the growth and processing technology of this material system, which have been validated from mass production, could compensate the residual degradation caused by mismatch adequately, makes this ternary very attractive from the application point of view. In the lattice mismatched system of $In_xGa_{1-x}As$ (x>0.53) on InP, some options of different buffer materials exist with different essential points of concern.

Fig.2 shows the lattice constant and bandgap energy contours of the InGaAsP quaternary, where InGaAs is at the top. As a natural choice, the InGaAs itself is a buffer layer option. The Indium composition x of $In_xGa_{1-x}As$ could be increased gradually from 0.53 to a desired value of y (corresponding to desired cutoff wavelength) in a continuous or step manner, on this buffer the PD structure could be grown. Generally, this scheme should be easier to realize without adopting other sources. Wavelength extending InGaAs photodetectors using $In_xGa_{1-x}As$ buffer have been grown by using MOVPE (e.g.: Moseley et al., 1986) or GSMBE (e.g.: Zhang et al., 2005, 2006a, 2006b) methods with different types of buffer and cap layer structures, and their performances were well evaluated. For the PDs normally a cap layer lattice matched to the light absorption layer is needed, in this scheme using also the composition y for the cap layer material with the same bandgap as that of absorption layer to form a homo pn junction is a rational choice. However, normally the cap layer using wider bandgap material is preferable to reduce the carrier loss due to the surface recombination, also to enhance the response at short wavelength side. Furthermore, in array applications the chip is often flip chip bonded to readout integrated circuit (ROIC), therefore back-side illumination is often adopted thus wider bandgap materials are also needed for the buffer layer to eliminate the absorption. In the InGaAsP system though using quaternary material as buffer is possible, taking care of four elements in the growth certainly is unnecessary, therefore the ternary InAsP is a good choice for the wider bandgap graded buffer. InAsP is also an alloy of two direct bandgap binaries InAs and InP with direct bandgap in full region. The lattice constant of InAsP can be changed from that of InP to InAs

thus it can be lattice matched to $In_xGa_{1-x}As$ for x>0.53 and have a wider bandgap than that of InGaAs lattice matched to it, so it is suitable for both the buffer and cap layers. The wavelength extending devices are used mainly for sensing purpose where response speed is not an important trait of concern, so the carrier accumulation at the heterointerface is not important.
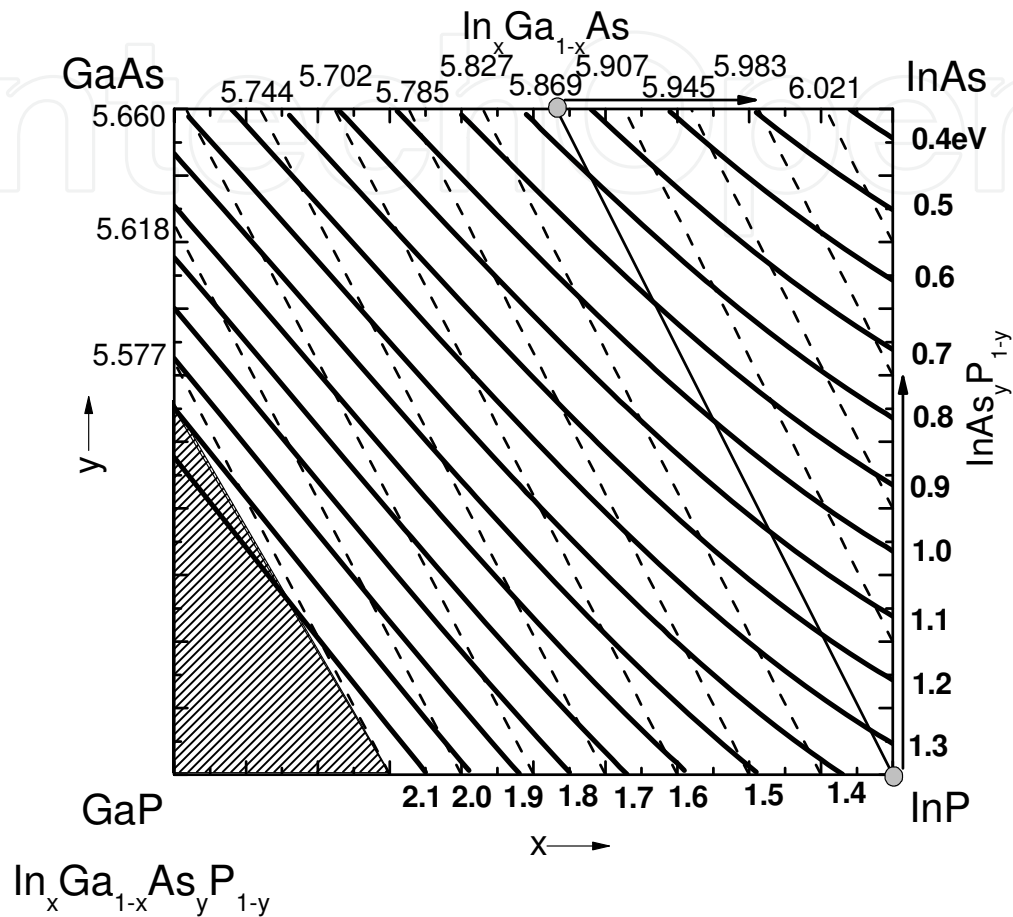

Fig. 2. Lattice constant and bandgap energy of InGaAsP quaternary system, the left bottom corner indicates the indirect bandgap zone.

From Fig.2 an example could be given. As buffer layer of $In_{0.8}Ga_{0.2}As$ active absorption layer with bandgap of about 0.5 eV cutoff at about 2.5 μm, the As composition in InAsP should be increased gradually from 0 to about 0.6; at this composition the bandgap of InAsP is about 0.75 eV, much wider than that of $In_{0.8}Ga_{0.2}As$. The InAsP is composed of two group-V elements As and P, indubitably in the growth these two sources should be needed and their ratio needs to be controlled effectively. Wavelength extending InGaAs photodiodes grown by using hydride vapor phase epitaxy (HVPE) (e.g.: Makita et al., 1988; Hoogeveen et al., 2001) or MOVPE (e.g.: di Forte-Poisson et al., 1992; Hondt et al., 1998) methods with different type of buffer and cap layer structures have been reported, and their performances were well evaluated. Note that in the lattice mismatched PD structure normally the buffer layer needs to be thick enough to reach a full relax. The growth of such materials with two group V components using vapor phase epitaxy is quite feasible, however, using molecular beam epitaxy (MBE) to grow such materials should be a challenge especially for thick layers. In MBE, setting the parameters to control two group V sources continuously and

simultaneously will be very difficult in spite of using gas source or solid source, regardless various other demands of the photodiode structures.

Other options can be explored from the $Al_zGa_xIn_yAs$ (x+y+z=1) quaternary system, Fig.3 shows the lattice constant and bandgap energy contours of this quaternary system. This quaternary system is composed of three group-III elements of Al, Ga and In, therefore As is the only group-V element. In this system the ternaries $In_xGa_{1-x}As$ and $In_xAl_{1-x}As$ are at the right and left ridge, their direct bandgap at 300K could be written as $E_g=0.36x+1.43(1-x)-0.477x(1-x)$ and $E_g=0.36x+3.03(1-x)-0.7x(1-x)$ respectively. From Fig.3 it is remarkable that, the lattice constant grid is almost horizontal in this system, which means for AlGaInAs quaternary with the same Indium composition the lattice constant is almost the same. In the AlGaInAs system though using quaternary material as buffer is also possible, but work with three group-III elements simultaneously will increase the complexity in the growth without benefit, therefore the ternary InAlAs becomes a superior buffer choice. The ternary $In_xAl_{1-x}As$ is the alloy of two binaries of direct bandgap InAs and indirect bandgap AlAs; therefore it becomes indirect bandgap material when the Al composition exceeds about 60%. At Indium composition x of 0.52% this ternary lattice matched to InP substrate with a quite wide bandgap of 1.47 eV at 300K, even wider than that of GaAs. From Fig.3 it could be seen, using $In_xAl_{1-x}As$ as buffer layer of $In_{0.8}Ga_{0.2}As$ active absorption layer with bandgap about 0.5 eV cutoff at about 2.5 μm, the In composition in InAlAs should be increased gradually from 0.52 to 0.8 likewise; at this composition the bandgap of InAlAs is about 0.78 eV, even wider than that of InAsP at the same lattice constant. The InAlAs is composed of two group-III elements In and Al, indubitably in the growth these two sources should be
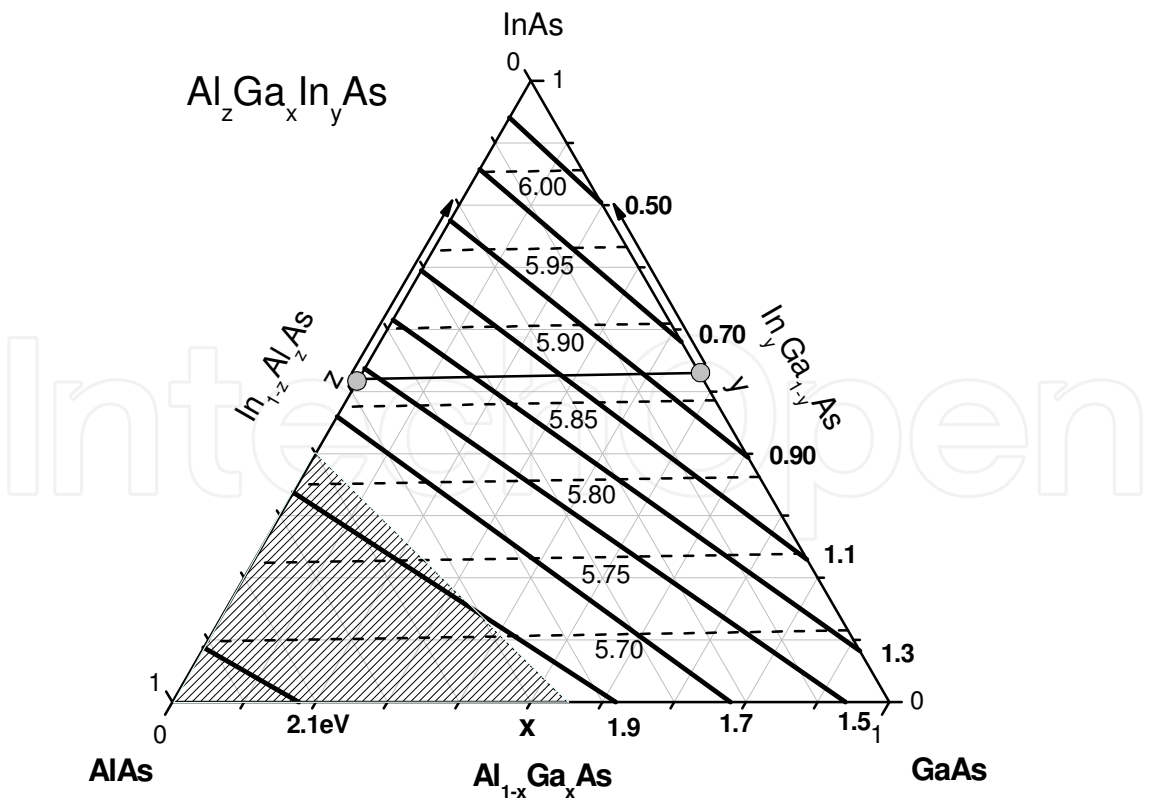

Fig. 3. Lattice constant and bandgap energy of AlGaInAs quaternary system, left bottom corner is the indirect bandgap zone.

needed and their ratio needs to be controlled effectively. Note that this is quite feasible in MBE. Besides, in this PD structure only InGaAs and InAlAs are adopted and in the epitaxial growth the phosphorus source is only used at pre-heat and desorption stage to protect InP substrate, therefore it is also feasible for the solid source MBE system without phosphorus source where arsenic flux may also be used for protection purpose. At the moment the solid source MBE system adopting solid phosphorus source is becoming popular, where this PD structure is also beneficial to save the phosphorus source. The lower Al composition <52% used in the wavelength extending PD structure will cause no reliability problem, and therefore it should be suitable for both the buffer and the cap layers. Wavelength extending InGaAs PDs grown on InP by using GSMBE (e.g.: Zhang et al., 2008a, 2008b, 2009a, 2009b, Tian et al., 2008b; Wang et al., 2009; Li et al., 2010; Gu et al., 2010) methods with different type of InAlAs buffer and cap layer structures have been reported, and their performances were well evaluated. These types of PDs even have been grown on GaAs substrate with even higher mismatch (e.g.: Zimmermann et al., 2003).

2.2 Gas source MBE growth of PD structures

In our works, two kinds of PD structures denoted as homostructure (where all the buffer, absorption and cap layers are InGaAs alloy) or heterostructure (where buffer and cap layers are InAlAs alloy, absorption layer is InGaAs alloy) were grown. All the epi-wafers in this work were grown by using a VG Semicon V80H GSMBE system. Photodetector wafers of various structures with different doping level in the $In_yGa_{1-y}As$ active absorption layer have been grown, where the In composition y is at desired value in the range from 0.6 to 0.9. In the growth, the elemental In, Ga and Al were used as group III sources, and their fluxes were controlled by changing the cell temperatures. Arsine (AsH_3) and phosphine (PH_3) high pressure cracking cells were used as group V sources (phosphorus source is only used for substrate protection purpose at pre-heat treatment stage), their fluxes were pressure controlled, and the cracking temperature was around 1000°C. Standard Be and Si effusion cells were used as p and n type doping sources, and doping level was also controlled by changing the cell temperatures. The fluxes of Al, Ga and In were calibrated with an in situ ion gauge to reach expected composition as well as moderate growth rate around 1 μm/hour. Calibration growths and X-ray measurements were carried out for lattice matched conditions of $In_{0.53}Ga_{0.47}As$ and $In_{0.52}Al_{0.48}As$ and then the parameters of Ga/In and Al/In fluxes were determined for further growth. Certainly, for the homostructure Al source is not used.

Before growth, the pre-heat treatment of the substrate was carried out in phosphor pressure at desorption. The process of pre-heat treatment was in situ monitored by reflection high energy electron diffraction patterns to see desorption of the surface oxygen, and then the substrate temperature was 10-30 °C decreased to begin buffer layer growth. In the growth of continuously graded $In_xGa_{1-x}As$ or $In_xAl_{1-x}As$ buffer layer, the In/Ga or In/Al flux ratio were increased continually until the In content increases from 53% to the desired value y (80% here as an example), then the growth of the $In_{0.8}Ga_{0.2}As$ absorption layer started. The $In_{0.8}Ga_{0.2}As$ absorption layer was doped with Si at designed level in the range between 1E16 cm^{-3} to 1E17 cm^{-3} according to the calibration data. After that, the Be doped $In_{0.8}Ga_{0.2}As$ or $In_{0.8}Al_{0.2}As$ cap layer was grown. The grown samples all have quite similar morphologies as shown in Fig.4 regardless of the final compositions. Under eye it has shiny surface, but with optical microscope the cross ripple could be seen along the <011> and <01$\bar{1}$ > directions,

which are typical morphology related to the existing of mismatch dislocations, especially at large positive mismatched conditions.
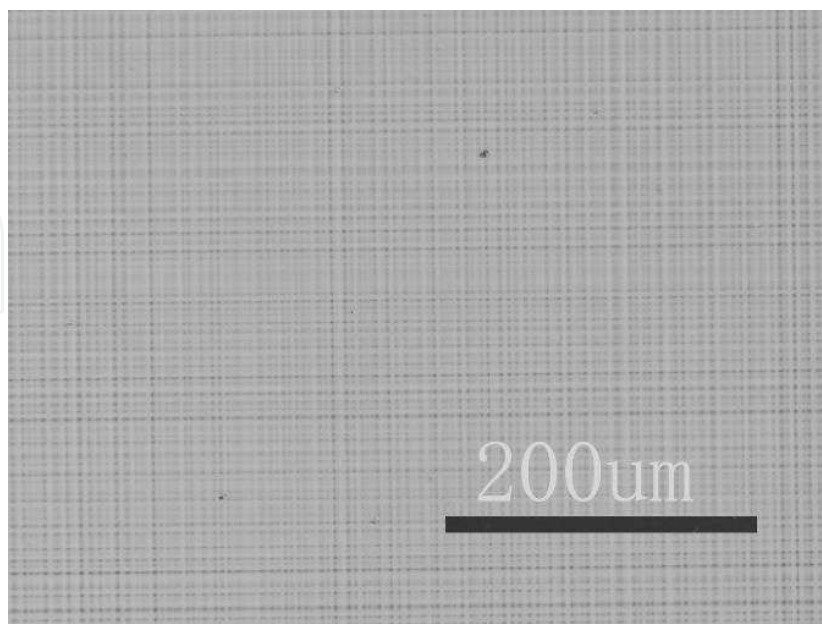

Fig. 4. Typical normasky micrograph of a GSMBE grown wavelength extending InGaAs detector epi-wafer with cross ripple pattern morphology, this wafer using 1 μm InGaAs continuously graded buffer with Indium composition of 0.6 in the absorption layer (Zhang et al., 2005).

In the growth of homostructure or heterostructure photodetectors with quite large lattice mismatch to the substrate, normally thicker layer with large lattice mismatch is desired, in this case the calibration growth of bulk layer will be quite difficult, and even possibly the calibrated data is not precise. We noticed that in the MBE growth the Ga and Al have almost the same flux characteristics and stick efficiency, but quite different from those of In. Based on this, a convenient and reliable growth procedure with excellent feasibility is developed, in which only the growth parameters of lattice matched $In_{0.53}Ga_{0.47}As$ and $In_{0.52}Al_{0.48}As$ are needed, that is: In the growth of all layers the As flux was kept constant, the growth of continuously graded $In_xGa_{1-x}As$ or $In_xAl_{1-x}As$ buffer begins from lattice matched condition of In/Ga or In/Al cell temperatures, T_{In}/T_{Ga} or T_{In}/T_{Al} (here T_{In} is the same for both InGaAs and InAlAs), then increase and decrease the cell temperature of In/Ga or In/Al simultaneously for ΔT_1 and ΔT_2 respectively at a very slow but fixed ramp rate. When the cell temperatures of In/Ga and In/Al reach $T_{In}+\Delta T_1/T_{Ga}-\Delta T_2$ or $T_{In}+\Delta T_1/T_{Al}-\Delta T_2$ at the same time, the growth of InGaAs absorption layer begins with $T_{In}+\Delta T_1/ T_{Ga}-\Delta T_2$ to a desired thickness, then growth the InGaAs or InAlAs cap with $T_{In}+\Delta T_1/ T_{Ga}-\Delta T_2$ or $T_{In}+\Delta T_1/T_{Al}-\Delta T_2$ to fulfill the whole structure. In this procedure the desired cutoff wavelength of the PD is only determined by ΔT, in our experience high quality wafers could be grown just by simply setting $\Delta T_2=2\Delta T_1$, no other careful calibration was needed.

After growth, the wafers were processed into mesa type photodetectors. The mesas with different diameters were defined by using photolithography and wet etching, and then passivated using plasma enhanced chemical vapor deposition of Si_3N_4. The contacts were formed using photolithography, evaporation of metals and lift-off. After an alloy step, the wafer was lapped and diced into chips, then packaged for further measurements.

3. Buffer layer optimization for mismatched InGaAs on InP

Unlike some other devices where only layers with sub-critical thickness are needed and dislocation free layers can be obtained, normally the growth of wavelength extending PD structures with thicker layers is accompanied by the generation of misfit dislocations and therefore the degradation of crystalline quality. Accordingly, a suitable buffer layer between InGaAs active absorption layer and InP substrate plays a prominent role on the growth of wavelength extending PD. The material system, modality and thickness of the buffer layer are the most important traits of concern. An appropriate buffer layer should relax the strain sufficiently, prevent the propagation of threading dislocations formed during the relaxation process into the active layers, form a moderate smooth surface morphology suitable for further device processing, and retain the intrinsic structural, optical and electrical qualities of the active layers.

As discussed in section 2.1, InGaAs homojunction, InAsP and InAlAs heterojunction buffer layers are some possible options for wavelength extending InGaAs PD structures. Efforts have continued to optimize the modality and growth schemes of buffer layers. Some people prefer a continuously graded buffer as it inhibits the dislocations propagating toward the active layer effectively (e.g.: Zimmermann et al., 2003; Zhang et al., 2008a, 2008b, 2009a, 2009b); others choose a step graded buffer since the interfaces between the consequent layers could bend the dislocation into the plane of growth (e.g.: Moseley et al., 1986; Makita et al., 1988; di Forte-Poisson et al., 1992; Hondt et al., 1998); strained-layer superlattice between steps is also adopted to filter threading dislocations (e. g.: Wada et al., 1993).

3.1 Continuously graded buffer of $In_xGa_{1-x}As$ versus $In_xAl_{1-x}As$

By MBE technology, the temperature ramping of the solid source beam flux to control the composition at high precision is more effective than the mass flow or pressure control in vapor phase epitaxy. Thus the $In_xGa_{1-x}As$ or $In_xAl_{1-x}As$ continuously graded buffer layers are feasible schemes in MBE. Comparing between $In_xGa_{1-x}As$ and $In_xAl_{1-x}As$ graded buffer layers, InAlAs heterojunction buffer with wider bandgap should be more appropriate for the reduction of carrier loss and FPA applications, whereas InGaAs homojunction buffer is generally considered to get better material quality if only from the material point of view. To evaluate the material quality of wavelength extending InGaAs PD structures using $In_xGa_{1-x}As$ or $In_xAl_{1-x}As$ continuously graded buffer layers in experiments, two PD structures with In content of about 0.78 in the InGaAs active absorption layer for the cutoff wavelength around 2.4 μm were grown on InP substrate by GSMBE with a grading rate of 0.6%μm^{-1} in the buffer layers, their characteristics were investigated and compared by the measurements of AFM, x-ray diffraction, TEM and PL.

The AFM images with 40×40 μm^2 scan area are shown in Fig. 5. The cross-hatch pattern could be attributed to the two types of misfit dislocations A and B oriented along the [1-10] and [110] directions, corresponding to group V and III atom-based cores, respectively (Wel et al., 1992). Along the [1-10] direction, the primary ridges are in parallel, and the period of primary ridges is around 5 μm. On the ridges small undulations exist periodically and the oval-like defects pop out on the top of the ridges. The period of the small undulations is around 1 μm. The surface morphology of sample (b) with InAlAs buffer appears to be more irregular than that of sample (a) with InGaAs buffer, which is due to the lower surface mobility of the Al atoms (Chyi et al. 1996). In spite of the more irregular morphology of sample (b), the root mean square (RMS) roughnesses of the two samples are nearly the same with 8.2 nm and 8.7 nm for

sample (a) and (b), respectively. It is inadequate to judge the qualities of the samples from morphology analysis alone, and further evaluations are needed.
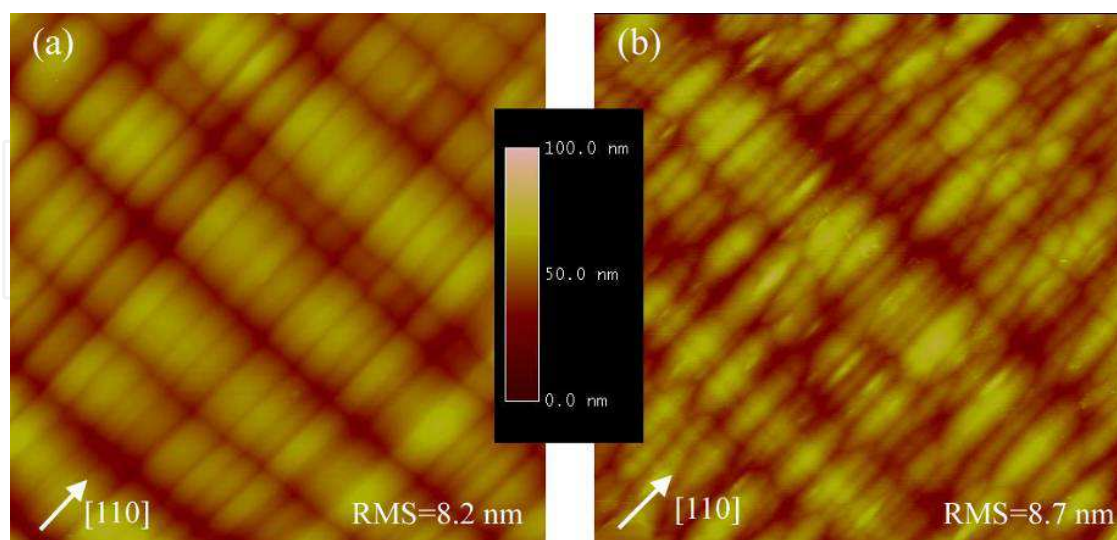

Fig. 5. AFM images of wavelength extending InGaAs PD structures with continuously graded (a) $In_xGa_{1-x}As$ and (b) $In_xAl_{1-x}As$ buffer layers.

To characterize the structural properties of the samples, x-ray diffraction reciprocal space mapping (RSM) and cross-sectional TEM measurements were used. The (004) and (224) RSM reflections were shown on the left side of Fig. 6. The intensities are in the logarithmic scale. In all RSMs, the relatively narrow and circular peaks correspond to the InP substrate (denoted as S). In Fig. 6(a), the relatively elliptical peak corresponds to the InGaAs absorption and cap layer of sample (a) (denoted as L), with a larger diffuse scattering perpendicular to the normal line due to the existence of dislocations. In Fig. 6(b), the diffraction features from InGaAs and InAlAs individual epitaxy layers adjacent with almost the same In contents are distinguished in the RSMs of the sample with InAlAs buffer. The two elliptical layer peaks correspond to the InGaAs absorption layer (denoted as L1) and InAlAs cap layer (denoted as L2) respectively. Those layers show diffusely scattered intensity patterns around reciprocal lattice point maxima, which results from the structural imperfections that can potentially degrade the material quality. L1 and L2 were assigned by measuring the HRXRD rocking curves in the same directions before and after the etching of the InAlAs cap layer. The layer peak was shifted toward the substrate side after the etching. On the (004) reflections, the divergencies of the centers of layer peaks and substrate peaks along the horizontal direction correspond to the macroscopic tilts of the layers to substrates (Fewster, 1993). The tilt angle of InGaAs absorption layer to the substrate is -26.4˚ and 1.1˚ for sample (a) and (b), respectively. For the (224) reflections, the intensities of substrate peaks are weaker than layer peaks due to the thick epi-layers and the weaker diffraction intensity from asymmetric (224) diffraction. The parallel mismatch and perpendicular mismatch of the InGaAs absorption layer were extracted from the RSMs, and then the cubic lattice mismatch, In composition, the degrees of relaxation and residual strain of the InGaAs absorption layer have been calculated and listed in Table 1. The degrees of relaxation are both larger than 90% for sample (a) and (b). It is noted that the residual strain in sample (a) is significantly larger than the calculated value from Turnoff's model (Tersoff, 1993). This suggests that a high tilt angle may be concurrent with a high residual strain. A possible

explanation is that if the material has a significant residual strain, the lattice needs to tilt itself in order to reduce the elastic strain energy. This is consistent with the proposition of some people (e. g. Lee et al., 2007) that elastic strain can be released by lattice tilt. On the other hand, the tilt angle and residual strain of sample (b) is really slight. The different behavior between sample (a) and (b) may be due to the large composition variation of sample (a) caused by the phase separation (Quitoriano et al., 2007).

Sample	Tilting Angle (°)	Indium content (%)	Perpendicular mismatch (%)	Parallel mismatch (%)	Cubic mismatch (%)	Degree of relaxation (%)	Residual strain (10^{-3}) XRD	Tersoff
(a)	-26.4	77.5	2.31	0.58	1.69	93. 7	-11	3.1
(b)	1.1	77.0	1.62	1.69	1.65	96.1	0.34	3.0

Table 1. Results from XRD RSM measurements for InGaAs absorption layer of the two samples.

The occurrence of phase separation for sample (a) was confirmed by TEM measurements as shown in right side of Fig. 6. The defects have been both reduced significantly in InGaAs absorption layer on the $In_xGa_{1-x}As$ and $In_xAl_{1-x}As$ graded buffer layers. In the graded buffer layers, most misfit dislocations are localized at the internal interfaces. Less misfit dislocations appear to propagate vertically through the structure in the $In_xAl_{1-x}As$ buffer
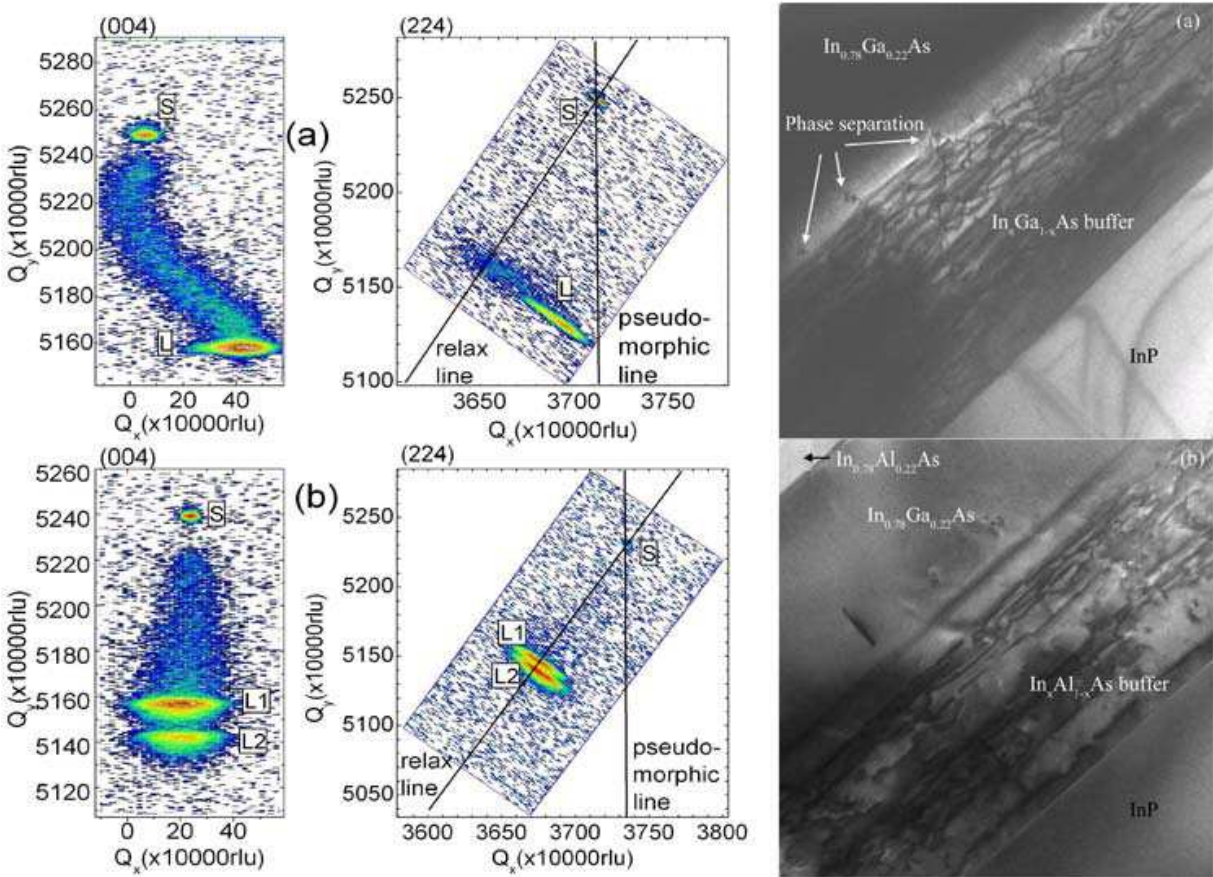

Fig. 6. RSM and cross-sectional TEM images of wavelength extending InGaAs PD structures with continuously graded (a) $In_xGa_{1-x}As$ and (b) $In_xAl_{1-x}As$ buffer layers.

layer than in $In_xGa_{1-x}As$ buffer layer. At the interface of $In_xGa_{1-x}As$ graded buffer and InGaAs absorption layer in sample (a), some diffraction contrast regions can be observed, which corresponds to the composition fluctuation induced by phase separation, whereas no obvious phase separation is observed in sample (b). It is probably due to the lower phase separation critical temperature of InGaAs than that of InAlAs (Quitoriano et al., 2007). The growth temperature is possibly located in the phase separation temperature region of InGaAs, whereas below the region of InAlAs.

The optical characteristics of the samples, which are correlated to the performance of the optoelectronic device in a more straightforward way, were evaluated using PL measurements at room temperature after etching away the cap layers. As shown in Fig. 7, both of the two samples show a PL peak from InGaAs absorption layer at about 2.41 μm. The PL intensity of sample (b) is more than twofold of sample (a) at room temperature. This indicates the improved optical characteristics and less presence of non-radiation recombination centers for the PD structure with $In_xAl_{1-x}As$ graded buffer layer.
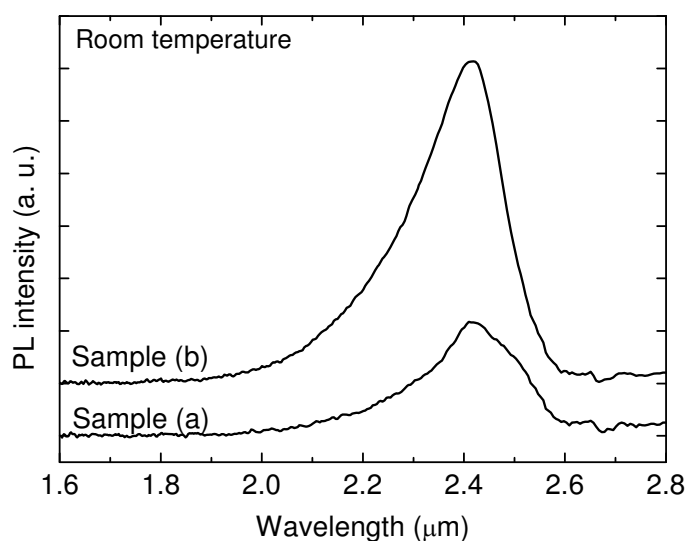

Fig. 7. PL spectra at room temperature of wavelength extending InGaAs PD structures with continuously graded (a) $In_xGa_{1-x}As$ and (b) $In_xAl_{1-x}As$ buffer layers, after etching away the cap layers.

As depicted in section 4.2, lower dark current and higher zero bias resistance area products R_0A could be obtained by using $In_xAl_{1-x}As$ heterojuction instead of $In_xGa_{1-x}As$ homojunction graded buffer and cap layer, which was attributed to the reduced carrier loss as the wider bandgap of InAlAs. It is believed that the reduced residual strain and decreased non-radiation recombination centers of the PD structure with $In_xAl_{1-x}As$ graded buffer layer should be also beneficial for the improvement of device performances.

3.2 $In_xAl_{1-x}As$ buffers at different grading rate

Generally, the buffer layers should be thick enough so that they become favourable for misfit dislocation to form and relax the buffer toward its freestanding lattice parameter. In vapour phase epitaxy, the achievable high growth rate makes the use of a thick buffer

appropriate; buffer thickness exceeding 10 μm is ordinary. However, the growth of an optically and electrically inactive buffer layer with excessive thickness is not only cost ineffective but also impractical sometimes, especially for the MBE where the actual growth rate is limited to around 1 μmh^{-1}. Therefore from practical point of view a thin buffer should be more preferable.

To evaluate how thin the buffer layer can be shrunk, $In_{0.78}Ga_{0.22}As$ PD structures for the cutoff wavelength around 2.4 μm were grown on InP substrate by GSMBE with continuously graded $In_xAl_{1-x}As$ (x=0.52 to 0.78) buffer and $In_{0.78}Al_{0.22}As$ cap layer. The thicknesses of the buffer layers are set to be 0.7 μm, 1.4 μm and 2.8 μm for sample (a), (b) and (c), corresponding to the lattice mismatch grading rate of 2.4, 1.2 and 0.6 %μm^{-1} respectively. As a reference, a lattice matched PD structure annotated as sample (d) was also grown, with a 0.5 μm N$^+$ InP buffer, a 2.5 μm n$^-$ $In_{0.53}Ga_{0.47}As$ absorption layer and a 0.6 μm P$^+$ InP cap layer.

Fig. 8 up right shows the AFM images with 40×40 μm^2 scan area measured in contact mode. In AFM images the cross-hatch pattern along [1-10] and [110] directions can be seen clearly. The RMS roughness for sample (a) with 0.7 μm buffer is 6.6 nm. With the double of buffer thickness, the RMS roughness increases to 9.5 nm for sample (b), and keeps almost unchanged of 9.7 nm for samples (c) with fourfold buffer thickness. Compare to the RMS roughness below 1 nm for the lattice matched structure sample (d), the mismatch induced morphology degradation is obvious. Results show that for the mismatch grading rate range from 2.4 to 0.6%μm^{-1} moderate roughness below 10nm could be reached, for further device processing this roughness is tolerable. Nevertheless it is inadequate to judge the quality of the wafer from the morphology analysis alone.

To determine the structural properties of the grown wafers, X-ray diffraction RSM analysis was applied. Fig. 8 left shows the RSMs from the symmetric (004) and asymmetric (224) reflections. In all RSMs, the relatively narrow and symmetric circular peaks correspond to the InP substrate (denoted as S). Other two predominant elliptical peaks, which are belong to the InGaAs absorption layer (denoted as L1) and InAlAs cap layer (denoted as L2) can be clearly distinguished. From the left side of Fig. 8, the (004) diffraction intensity maxima for each layer is almost centered on the substrate reciprocal lattice points along the vertical line, indicating minimum lattice tilt with respect to the substrate. The tilt angles of L1 to the substrate are -1.8°, -5.6° and -1.1° for sample (a), (b) and (c) respectively. From the asymmetric (224) reflection the contours of layers are all far from the pseudomorphic line, indicating that the strain has been relaxed through the continuously graded buffer. For sample (b) and sample (c) the intensity contours corresponding to InGaAs absorption layer L1 are centered on the relaxation line symmetrically, indicating the full relaxation of the layer. However, for sample (a) with the highest mismatch grading rate of 2.4%μm^{-1} the intensity contours corresponding to the InGaAs absorption layer L1 is apart from the relaxation line, makes an angle of 30.7° with respect to the vertical substrate reciprocal lattice intensity contours, which indicating that this layer is not relaxed sufficiently, since the angle between (004) and (224) should be 35.2° for a full relaxed layer. From the (224) reflection the In content, perpendicular mismatch and parallel mismatch of the layer L1 are extracted as listed in Table 2. The cubic lattice mismatch and degree of relaxation of the layer L1 are then calculated as also listed in Table 2. For both sample (b) and (c) the degree of relaxation reaches 102% whereas for sample (a) the value is 95%, regardless of the experimental error. In Table 2 the calculated residual strain at the interface of graded In_xAl_{1-}

$_x$As buffer to In$_y$Ga$_{1-y}$As (L1) absorption layer by using Turnoff's model were also listed (Tersoff 1993). Comparing the residual strain and In composition data in Table 2, an alloy concentration setback effect could be clearly seen. For sample (a) with higher grading rate the residual strain at the interface pullback the In composition distinctly, the trend consists with Turnoff's model well.
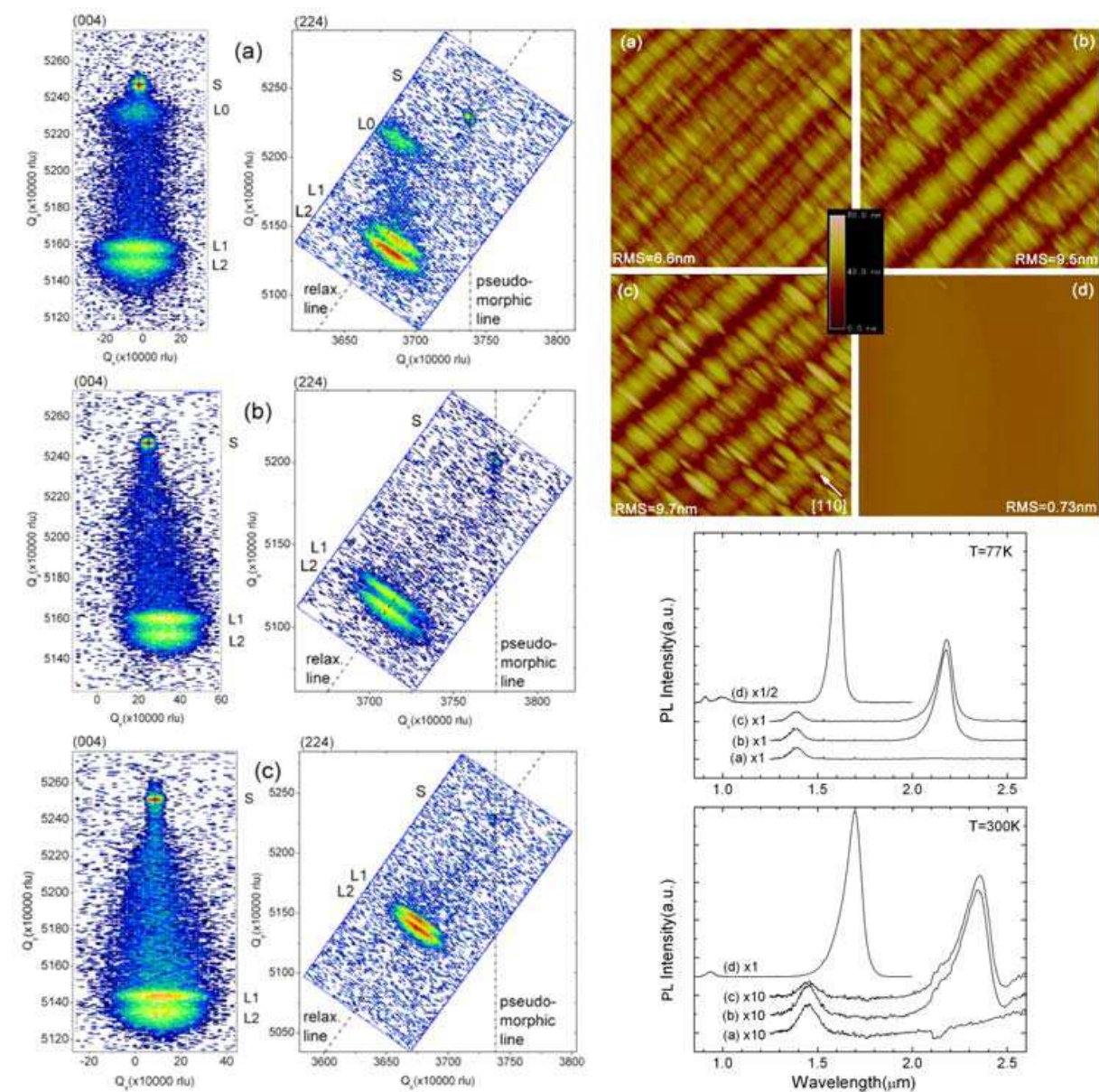

Fig. 8. RSM, AFM and PL spectra of wavelength extending InGaAs PD structures with continuously graded In$_x$Al$_{1-x}$As buffer at different grading rate.

It is noticed from the RSMs that two types of relax mode may exist. From (004) reflections, the presence of continuously graded buffer can be noticed in the region between S and L1. For sample (b) and sample (c) in this region a pattern along Q_y direction appears diffusely, the mosaic structure is observable through a gradual extension along the Q_x directions, indicating a gradual relaxation process of the lattice. However, for sample (a) in this region the pattern is more uniform, a thin layer (denoted as L0) appears, which shows a weaker

reflecting signal compare to L1 and L2. Note that this layer is unintentionally grown. From the (004) reflection L0 is quite close to the substrate. According to (224) reflection, a very weak pattern between L0 and L1 exists, which is almost parallel to the pseudomorphic line respect to L0 and L1. Detailed analysis from (224) reflection shows that L0 is almost fully relaxed in the parallel direction with respect to the substrate, while remaining strained along the perpendicular direction. This phenomenon prompts that when the grading rate during the growth becomes too high, an intermediate layer may form to release the strain in two steps. In this case, plenary relaxation of the subsequent layer will be difficult. The results reveal that in this type of structures containing thicker mismatched active layers, the grading rate is extremely important to the totally relaxation.

The optical qualities of the epi-layers are evaluated using PL measurements. Fig. 8 down right shows the 300K and 77K results. The PL of the reference sample (d) is also shown, which show 5~10 times enhancement in the intensity. At room temperature, sample (b) and (c) show fair PL signals from the InGaAs absorption layer peaked at about 2.35 μm with the FWHM of about 50 meV, whereas for sample (a) with the mismatch grading rate exceeding 2%μm^{-1} no PL signal could be observed. For these three samples, the PL signals from the InAlAs cap peaked at about 1.45 μm are almost identical. At 77 K, the PL peaks blue shifted to around 2.18 μm with the FWHM of about 35 meV and the intensities increase more than 6 folds, but for sample (a) still no PL signal from the InGaAs layer could be found. Therefore at this exorbitant grading rate the relaxation process are definitely insufficient; the residual strain and dislocation give rise to nonradiative centers and defect-assisted minority carrier recombination, degrading the optical quality of the layer notably. Moreover, for sample (c) with the lowest grading rate of 0.6%μm^{-1}, no further improvement of the PL could be noticed compared to sample (b) with a doubled grading rate, indicating that for this wavelength extending PD structure with a continuously graded buffer layer, a mismatch grading rate around 1%μm^{-1} should be slow enough to reach favorable structural and optical qualities.

Sample	Buffer thickness / grading rate (μm)/(% μm^{-1})	Indium content (%)	Perpendicular mismatch (%)	Parallel mismatch (%)	Cubic mismatch (%)	Degree of relaxation (%)	Residual strain (10^{-3})
(a)	0.7/2.4	73.75	1.662	1.512	1.586	95.33	6.388
(b)	1.4/1.2	74.42	1.607	1.682	1.645	102.2	4.517
(c)	2.8/0.6	74.53	1.616	1.691	1.654	102.2	3.194

Table 2. Results from XRD RSM measurements for InGaAs absorption layer of samples (a), (b) and (c).

4. Performance of GSMBE grown wavelength extending InGaAs PDs

4.1 Homostructure PDs

The response spectra of the detector were measured by using a Nicolet Magna 760 Fourier transform infrared (FTIR) spectrometer; in the measurement CaF2 beam splitter and Ever-Glo IR source were used. The DUT detector chip was mounted on a Cu block and packing into a metal Dewar and its output signal was fed into the pre-amplifier of the spectrometer. Fig.9 shows the measured relative response spectra of detectors cutoff at about 1.9, 2.2 and 2.5 μm at 300K, denoted as (a), (b) and (c) respectively (1.9μm, 2.2μm and 2.5μm detector

hereafter), the detectors were under zero bias. For those detectors, homostructures with relatively thin graded layer were used. The epitaxy structure of the photodetectors consists of a 0.5μm n- InP buffer layer, a 1.0 μm (for a) or 1.5 μm (for b and c) n- $In_xGa_{1-x}As$ continuously graded buffer layer with x changes from 0.53 to y of 0.6, 0.7 or 0.8, a 2.5μm n- $In_yGa_{1-y}As$ absorbing layer and a 0.5μm p+ $In_yGa_{1-y}As$ top layer. The samples were grown on exactly (100) oriented n+ InP epi-ready substrates doped with S, their carrier concentration were about 2E18 cm-3. From Fig.9 it could be seen that, at 300K the detectors show response peaks at 1.86, 2.10 and 2.36 μm, with 50% cutoff wavelength of 1.90, 2.17 and 2.45 μm respectively. At 77K, the peaks blue shift to 1.68, 1.92 and 2.12 μm and cutoff at 1.72, 1.95 and 2.17 μm respectively, with temperature coefficients of 0.78, 0.99 and 1.25 nm/K in this temperature range. In the spectra, fluctuations around 1.87 μm as well as 1.38 μm, which are
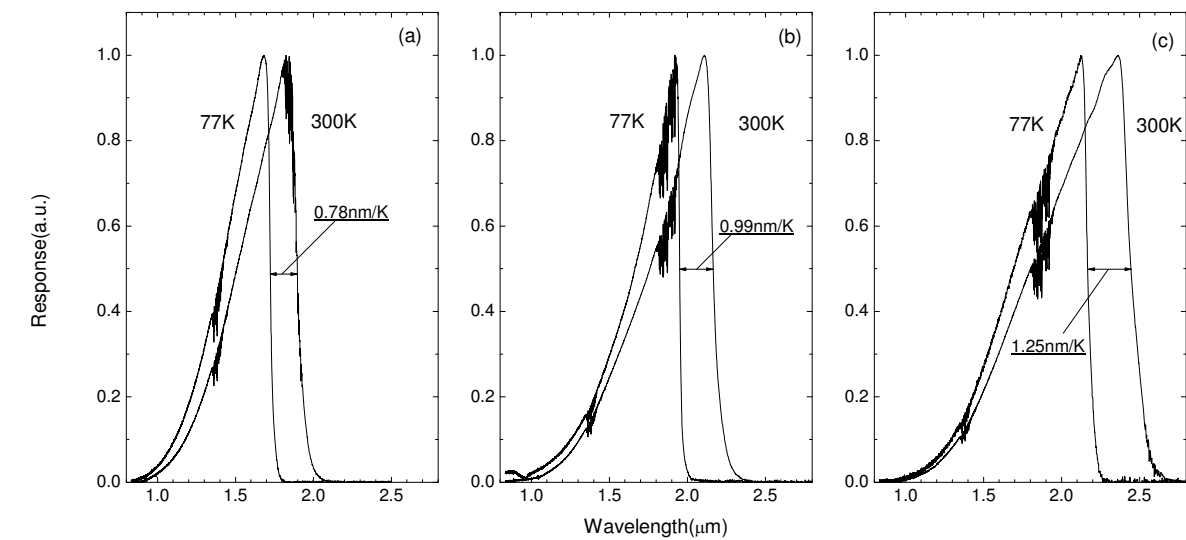

Fig. 9. Measured response spectra of the homostructure InGaAs PDs with cutoff wavelengths about (a)1.9μm , (b)2.2μm and (c)2.5 μm at room temperature.
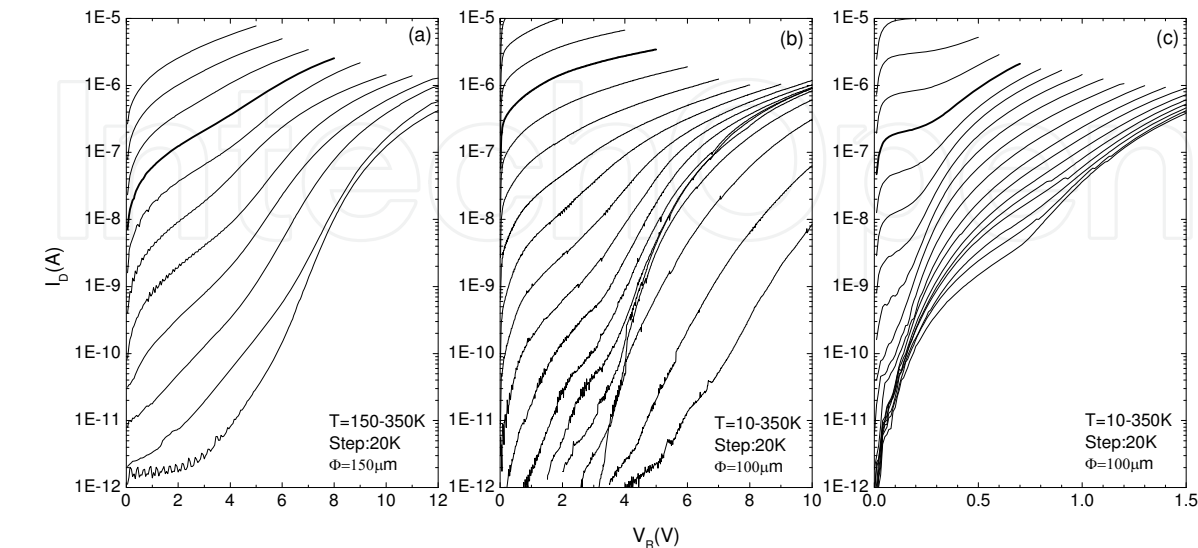

Fig. 10. Measured temperature dependent I-V characteristics of the homostructure InGaAs PDs with cutoff wavelengths about (a)1.9, (b)2.2μm and (c)2.5 μm at room temperature.

corresponding to the water vapor absorption band caused by trace vapor in the air along the optical path, could be clearly seen.

The temperature behaviors of the dark current, which are directly correlated to the performance of the detector, have been measured using a HP4156A precise semiconductor analyzer, in the measurements the detector chips were mounted into a DIP package and installed on the cold head of a closed cycle He cryopump to control their temperature. Fig.10 shows the typical I-V characteristics of the detectors measured in a wider temperature range up to 350 K with step of 20K and over 7 orders of magnitude in current range. It could be seen from Fig.10 that, the dark current of 1.9, 2.2 and 2.5 μm detectors are 2.9 nA, 57 nA and 67 nA at 290K respectively with reverse bias V_R=10mV, and decrease to 28 pA, 84 pA and 161 pA at 210K. To see the temperature dependence of the dark current more clearly, an Arrhenius plot was done with reverse bias voltages of 10 mV. At temperature range from about 210 K to 350 K, a fixed slope could be seen for those detectors, so in this temperature range the thermally activated dark currents, which could be expressed as $I_d \propto exp(-E_a/kT)$, are dominant, which means in this temperature range the Johnson noise is the main noise source to determine the detector performance. At V_R=10mV, activation energies E_a of 0.488eV, 0.447eV and 0.404eV could be deduced for 1.9 μm, 2.2 μm and 2.5 μm detectors respectively. Based on this data, an order of decrease in the dark current could be expected for those detectors by using one stage TE cooling. We also noticed that this activation energy is comparable but lower than the band gap of the material, so in this ternary alloys the detectors may have similar temperature features. At lower temperature, the dark current drops further but with a lower slope, and becomes constant below about 150K.
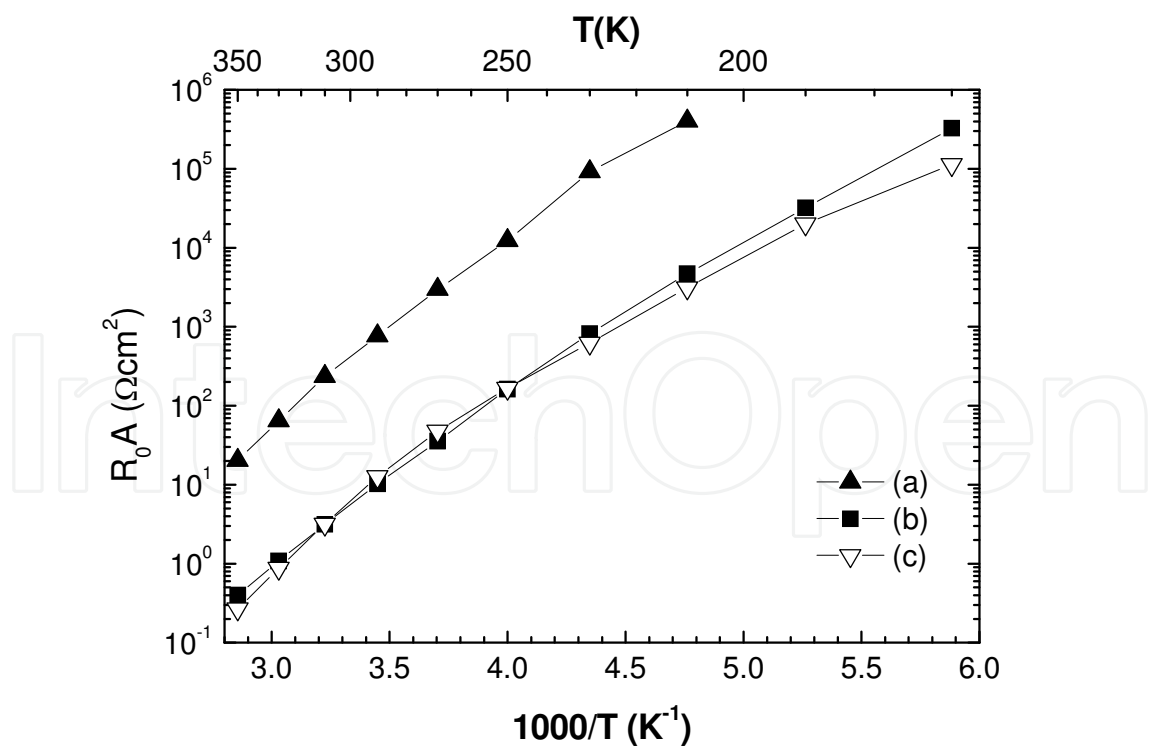

Fig. 11. Measured resistance area product R_0A versus reciprocal temperature of the homostructure InGaAs PDs with cutoff wavelengths about (a)1.9, (b)2.2μm and (c)2.5 μm at room temperature.

The shunt resistances of the detector at 0V bias R_0 are also measured, Fig.11 plots the resistance area product R_0A versus temperature of the detectors. At 290 K, R_0A of 765, 10.3 and 12.7 Ωcm^2 were measured for 1.9 µm 2.2 µm and 2.5 µm detector respectively. When the detectors were cooled down to 210K, the R_0A increased more than 2 orders to 404, 4.70 and 3.12 $K\Omega cm^2$ respectively. The calculated peak detectivity from the R_0A reached 2.3E11, 3.0E10 and 3.7E10 $cmHz^{1/2}/W$ at 290K, and increased to 5.6E12, 7.2E11 and 6.6E10 $cmHz^{1/2}/W$ at 210K respectively, in the calculation the quantum efficiency $\eta=0.7$ was supposed. From the measured results we also noticed that, at lower bias conditions and higher temperature region (e.g. T>200K), the performances of the this 2.5 µm detector are comparable to (or even slightly better than) that of 2.2 µm detector, this could be attributed to the slightly higher Si doping (higher electron concentration) in the InGaAs absorption layer of the 2.5 µm detector. From our analysis (Hao et al. 2006), at lower bias and higher temperature the dark current of the detector was dominated by the generation-recombination mechanism, so slightly higher carrier concentration in the InGaAs absorption layer could result in lower dark current and therefore higher R_0A. Whereas at higher bias and lower temperature, the tunneling mechanism becomes dominant and higher carrier concentration results in higher dark current. It means that the performance of the detectors can benefit from slightly higher doping in the absorption layer, especially for detectors mostly working at lower bias (or zero bias) conditions and higher temperature region. However, higher carrier concentration in the InGaAs absorption layer will decrease the depletion layer thickness, and therefore the quantum efficiency of the PDs (Tian et al. 2008a, 2008c). Notice that signal/noise ratio related detectivity, which is a figure of merit of the PDs, is decided by both R_0A and the quantum efficiency; therefore a tradeoff of the doping level in the absorption layer should be taken to optimize the performance. In most case, doping level of 2E16 - 5E16 cm^{-3} in the absorption layer is appropriate. In an optoelectronic system normally the PDs are connected to the ROIC or pre-amplifier directly, hence the noise of the electronics should be considered with those of PDs together. In the case of wavelength extending InGaAs PDs especially with longer cutoff wavelength and operating at higher temperature, the noise from the PDs will be dominant. Consequently, for the optimization of the system performance the R_0A or dark current is the first factor of concern. Those types of epi-wafers cutoff at 2.4 µm have been used for array applications where moderate performances have been reached (Zhang et al. 2007).

4.2 Heterostructure PDs

Fig. 12 shows the response spectra of two heterostructure PDs at zero bias, the PDs are with the cutoff wavelengths about 2.9, and 2.4 µm respectively at room temperature (denoted as sample A and sample B or 2.9µm and 2.4µm detector hereafter).

For those PDs, InAlAs graded layer were used. The epitaxy structure of the PDs consists of a 0.15 µm InP buffer, a 2.4µm N^+ $In_xAl_{1-x}As$ continuously graded buffer layer, the composition x is graded from 0.52 to y of about 0.9 or 0.78 for sample A and sample B respectively and carrier concentrations were about 2E18 cm^{-3}; a 2.0µm n^- $In_yGa_{1-y}As$ absorbing layer and a 0.6µm P^+ $In_yAl_{1-y}As$ cap layer with carrier concentration of about 2E18 cm^{-3}. The samples were grown on exactly (100) oriented S. I. InP epi-ready substrates. The response spectra of the PDs are similar to the homostructure PDs without noticeable difference. The response peaks are at 2.70 µm and 2.24 µm with 50% cutoff wavelength of 2.88 µm and 2.38 µm for sample A and sample B respectively at 300K.
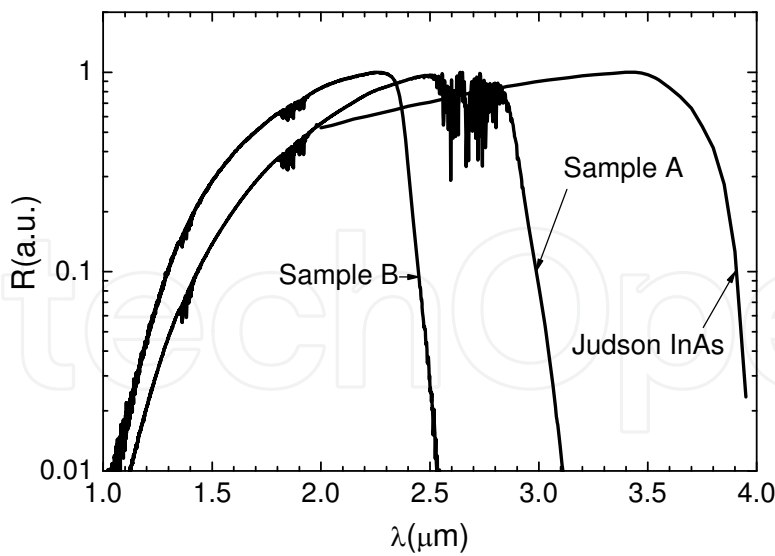
Fig. 12. Measured response spectra of the heterostructure InGaAs PDs with cutoff wavelengths about 2.9 μm (sample A) and 2.4 μm (sample B) at room temperature. (Judson InAs PD is for comparison).
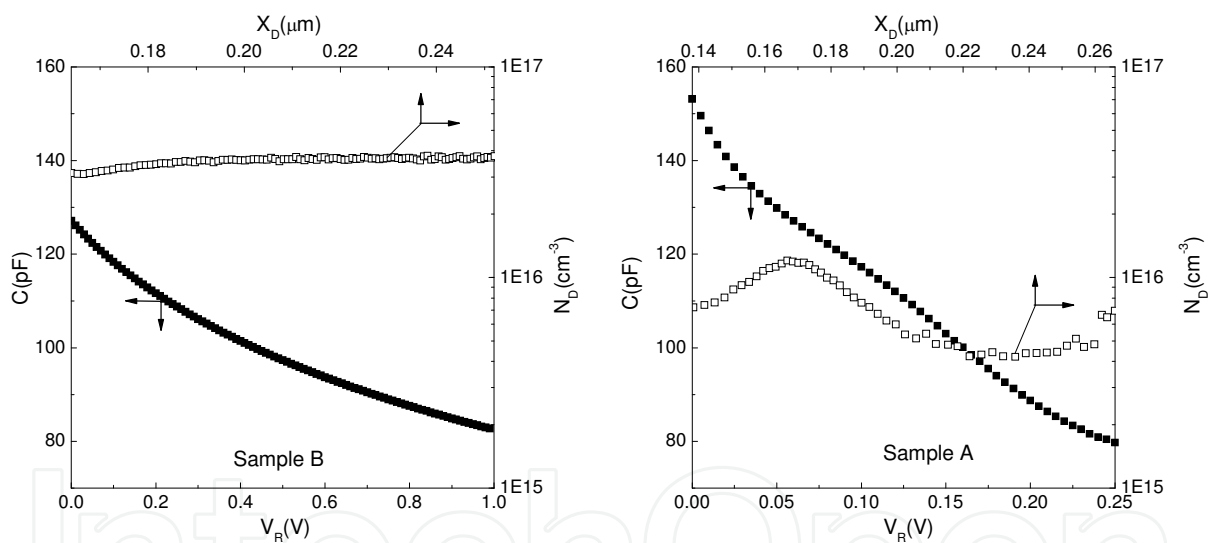

Fig. 13. Measured C-V characteristics of the PDs and calculated carrier concentration in the absorption layer of sample A and sample B.

Fig. 13 shows the C-V characteristics of the detectors measured at 300 K and 1 MHz, the diameters of the detector mesas are 500 μm. From Fig. 13 the capacitances at 0 V bias are 153 pF (78.1nF/cm²) and 127 pF (64.5nF/cm²) for sample A and sample B respectively. The electron concentrations educed from the C-V date are below 1E16 cm⁻³ for sample A and around 3E16 cm⁻³ for sample B by using N= $(1/q\varepsilon_0\varepsilon_r A^2)$ $[C^3/(dC/dV)]$ and $X_d=\varepsilon_0\varepsilon_r A/C$, where A and C are the area and capacitance of the detectors. It can be seen that at the same Si doping temperature sample A shows lower carrier concentration in the InGaAs absorption layer. One possible reason is due to the carrier depletion caused by the electrical inactivation of dopant and electron trap, for example, formed by misfit dislocations (Uchida et al. 1993).

Typical reverse I-V characteristics of the two heterostructure PDs measured at different temperature are shown in Fig. 14. The detector diameters of sample A and B are 300 μm and 500 μm respectively. The purpose to use a larger diameter for sample B is that the minimum measurable current on our cryostat system is on the order of 10 pA limited by EM interference, therefore a lower temperature could be reached if a larger diameter is used. The current features of those two samples with different cutoff wavelengths are quite different. For sample A at the reverse bias V_R=10 mV, the dark current decreases only about an order of magnitude from 2.0 μA (2.8E-3 A/cm^2) at 290 K to 0.14 μA (2.0E-4 A/cm^2) at 190 K, whereas for sample B the dark current decreases three orders of magnitude from 0.67 μA (3.4E-4 A/cm^2) at 290 K to 456 pA (2.3E-7 A/cm^2) at 190 K, so the current transport mechanisms for those two samples should also be different. To see the dark current characteristics more clearly, Arrhenius plots of the dark current at -10 mV are made for both samples as shown in Fig. 15. For sample A, a fixed slope can be only seen at higher temperature range from about 250 K to 350 K, whereas current drop saturation can be clearly seen at lower temperatures. For sample B, fixed slope extends in whole measurement temperature range, no current drop saturation can be seen until 190 K. This means that, for sample B with lower Indium composition of x=0.78 and therefore shorter cutoff wavelength, at reverse bias of V_R=10 mV the thermally activated dark current, which is expressed as $I_d \propto \exp(-E_a/kT)$, is dominant in a wider temperature range. Activation energy of 0.46 eV can be deduced. However, for sample A with higher Indium composition of x=0.9 and cutoff wavelength at 2.9 μm, at reverse bias of V_R=10 mV the thermally activated dark currents only dominant at higher temperature range, where activation energy of 0.33 eV can be deduced.

The band gaps E_g of the InGaAs layers at room temperature are about 0.43 eV and 0.52 eV for sample A and B respectively. From the results it can be inferred that, at lower bias of 10 mV, the diffusion current may be the main current from above room temperature to lower
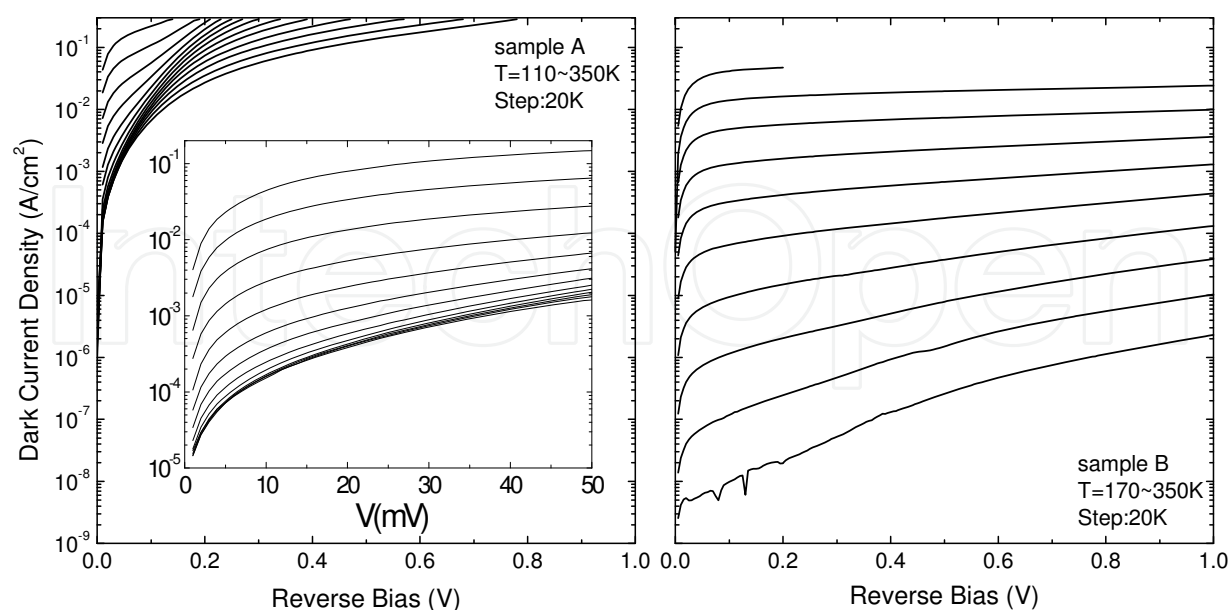

Fig. 14. Measured temperature dependent I-V characteristics of the heterostructure InGaAs PDs with room temperature cutoff wavelengths about 2.9 μm (sample A) and 2.4 μm (sample B).
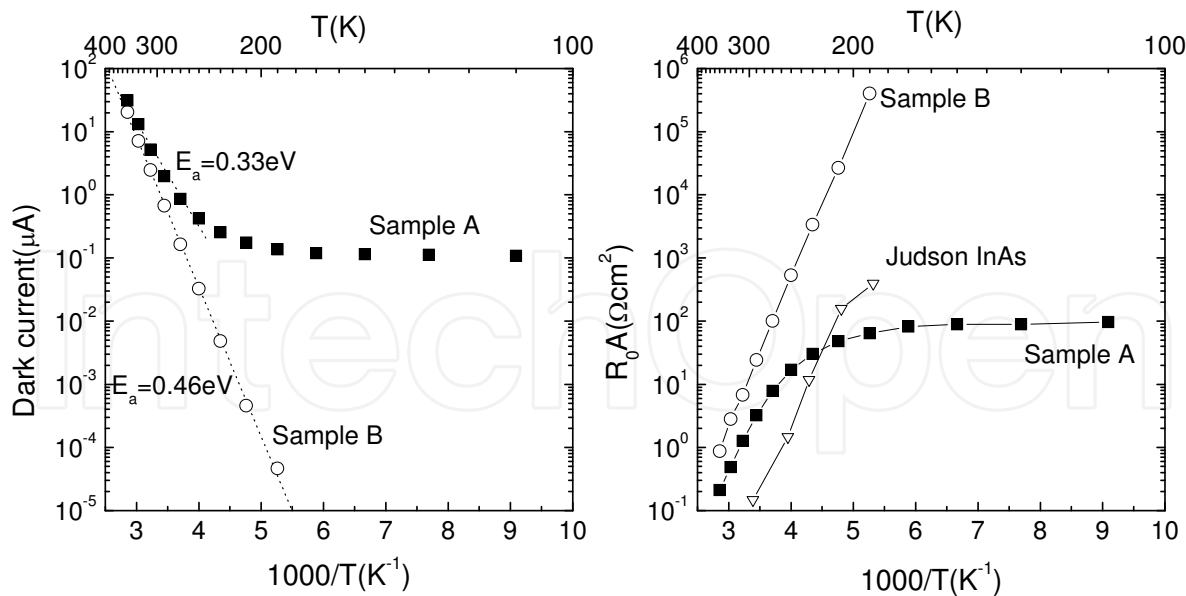
Fig. 15. Arrhenius plots of the dark current versus reciprocal temperature at reverse bias of 10 mV (left) and measured resistance area product R_0A versus reciprocal temperature (right) of the heterostructure InGaAs PDs with cutoff wavelengths about 2.9µm (sample A) and 2.4µm (sample B), for comparison the R_0A data of Judson InAs PD was also shown in the right, it cutoff at 3.6 µm at room temperature.

than 190 K for sample B because its E_a is more close to E_g, while for sample A from 250 K to 350 K, the G-R current and diffusion current both have important contributions. At temperature lower than about 250 K, the dark current of sample A decreases slowly. The thermal activated current at lower temperature decreases rapidly, also for our processing the ohmic leakage is not on this high level, meanwhile, at this lower bias of 10mV the direct tunnelling could also be eliminated. This means the trap assisted tunnelling current, which represents electrons tunnel from the occupied trap states to the empty band states, begins to play an important role. From above results, the performances of 2.9 µm InGaAs detectors seem still quite competitive at higher operation temperatures until about 250 K, but the effects of further decreasing the operation temperature to improve the performances of the detectors will be limited, mainly because of the trap states caused by the large lattice mismatch related defects. Despite the lower energy gap of the material, larger lattice mismatch accelerates the degradation of the detector performances further.

The shunt resistances R_0 of the detectors at 0 V bias were also measured. Fig. 15 right shows the typical resistance area product R_0A versus reciprocal temperature. At 290 K, R_0A of 3.2 Ωcm² (R_0=4.5 kΩ) and 24 Ωcm² (R_0=12 kΩ) are measured for sample A and sample B, respectively. When the detectors are cooled down to 250 K, the R_0A increases exponentially to 17 Ωcm² (R_0=24 kΩ) and 534 Ωcm² (R_0=272 kΩ) for sample A and sample B. The R_0A of commercial Judson InAs detector is also shown in Fig. 4, with 0.15 Ωcm² (R_0=0.3 kΩ) at 295 K and 1.5 Ωcm² (R_0=3 kΩ) at 253 K respectively (detector diameter of 250 µm). It can be seen that the R_0A of 2.9 µm InGaAs detector is higher than lattice matched Judson InAs detector until about 220 K.

The black-body response measurements of the detectors were also performed at room temperature with a T_B=900 K black body. The measured peak detectivity $D^*_{\lambda p}$ of 2.9 µm detector (sample A) is 6.6E9 cmHz$^{1/2}$/W, while for 2.4 µm detector (sample B) is 3.1E10
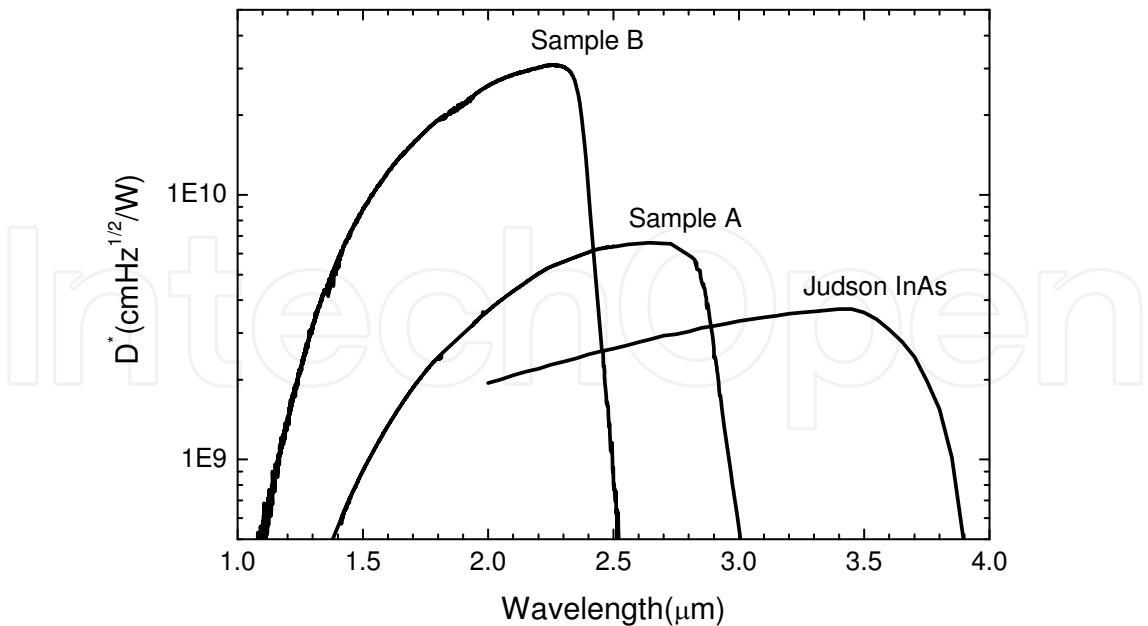
Fig. 16. Measured black body and peak detectivity versus wavelength of sample A and sample B (the spectra are smoothed) at room temperature. For comparison the data of Judson InAs PD was also shown.

$cmHz^{1/2}/W$, as listed in Table 3. Moreover, the wavelength dependent detectivity of the detectors for sample A and sample B at room temperature are shown in Fig.16. In Fig.16 the response spectra are smoothed to eliminate the water absorption bands. The detectivity spectrum of Judson InAs detector at room temperature is also shown in Fig.16 for comparison, which has a value of 3.7E9 $cmHz^{1/2}/W$ at response peak about 3.45 µm. At wavelength of 2.65 µm, the detectivity of sample A reaches 6.6E9 $cmHz^{1/2}/W$, twice that of Judson InAs detector of 2.9E9 $cmHz^{1/2}/W$ at the same wavelength. From Fig.16 it could be inferred that, extending the cutoff wavelength of InGaAs detectors on InP substrate up to about 3 µm is still quite valuable. Therefore for certain applications where the cutoff wavelength less than 3 µm is enough, this detector is still a good choice especially at high operation temperatures. Furthermore, the wavelength extending InGaAs detectors grown on InP substrate are very suitable for the array integration illuminated from the substrate (back) side, where the detector arrays are often connected to the read-out circuits using flip-chip bounding. The S. I. InP substrate is transparent to the detected light, whereas in this case the InAs substrate is opaque. However, for applications using discrete device at even longer wavelength, lattice matched InAs detector may be more suitable especially at lower operation temperatures, further extending the cutoff wavelength of InGaAs detectors remains a challenge. The PDs have been used for gas sensing purpose where good performances have been reached (Zhang et al., 2007b, 2008c).

Sample	V_s/V_n	g-factor	D^*_{bb} ($cmHz^{1/2}/W$)	$D^*_{\lambda p}$ ($cmHz^{1/2}/W$)
A (2.9µm)	1.4E3	7.0	9.4E8	6.6E9
B (2.4µm)	3.3E3	14	2.2E9	3.1E10

Table 3. Measured black body and peak detectivity of sample A and B at room temperature using a 900K Black body

4.3 n on p configuration.

In most array applications, illuminating from back side with Indium bump flip chip bounding to CMOS readout integrated circuit (ROIC) is much preferable, in this case the p-on-n configuration may not be a good choice. In p-on-n configuration, when the light is illuminated from substrate side (backside), the stronger absorption is also occurs at the absorption layer near the backside, where are away from the pn junction depletion region if the absorption layer is too thick, thus restrict the collection of the generated carriers. Furthermore, the response speed may also be affected because of the slower diffusion process. However, if the absorption layer is too thin, the full absorption of the illuminating light becomes impossible. Through the tradeoff of the absorption layer thickness in conjunction with the doping level the situation can be improved (Tian et al. 2008a, 2008c), but the optimization still be quite difficult. In certain array applications including earth observation the quantum efficiency or sensitivity are the most important trait of concern. Notice that normally the ROIC is suitable for both p-on-n and n-on-p polarities especially at small signal conditions, so instead of p-on-n the n-on-p configuration should be more preferable. Based on those considerations, heterostructure PDs with n-on-p configuration were constructed. Two photodiode wafers (Sample A of 2.0 μm device and Sample B of 2.4 μm device hereafter) with different In content y in the $In_yGa_{1-y}As$ absorption layer were grown. Epitaxial structure of the photodiode wafers began from a heavy Be doped P^+ $In_xAl_{1-x}As$ continuously graded buffer layer (thickness of 3 μm), its composition x was graded from 0.52 to a setting value of y and carrier concentration was about 2E18 cm^{-3}; afterwards, a n-$In_yGa_{1-y}As$ absorbing layer (thickness of 2.2 μm) with light doping of Si optimized to abort 3E16 cm^{-3} and a N^+ $In_yGa_{1-y}As$ contact layer (thickness of 0.2 μm) with heavy doping of Si to about 2E18 cm^{-3} were grown. In this experiment the samples were grown on exactly (100) oriented Zn doped P^+ InP epi-ready substrates, in fact for back illumination application the S. I. InP substrate is better for its much lower free carrier absorption.

Fig.17 left shows the I-V characteristics of the photodiodes measured in the temperature range from 150 K to 350 K with step of 20K and over 7 orders of magnitude in current range, the photodiode mesa diameters were 300 μm. For sample A at reverse bias V_R=10mV, the dark current was 11.3 nA(1.6E-5 A/cm^2) at 290K and decreased to 30.7 pA(4.33E-8 A/cm^2) at 210K; for sample B at reverse bias V_R=10mV, the dark current was 75.1 nA(1.06E-4 A/cm^2) at 290K and decreased to 102 pA(1.44E-7 A/cm^2) at 210K.

Meantime, an Arrhenius plot was done as shown in Fig.18 at reverse bias voltages of 10 mV. At temperature range from 210 K to 350 K, a fixed slope could be seen for both samples. In this temperature range the thermally activated dark currents, which could be expressed as $I_d \propto exp(-E_a/kT)$, are dominant. This implies that in this temperature range the Johnson noise is the main noise source to determine the performance. At reverse bias of 10mV, activation energies E_a of 0.4510eV and 0.4070eV were deduced for sample A and sample B respectively. The shunt resistances of the detector at 0V bias R_0 are also measured; Fig.18 plots the typical resistance area product R_0A versus temperature. At 290 K, R_0A of 760 Ωcm^2 (R_0= 1.07 MΩ) and 104 Ωcm^2 (R_0=147 KΩ) were measured for sample A and sample B respectively. When the photodiodes were cooled down to 210K, the R_0A increased more than two orders to 250 KΩcm^2 (R_0=354 MΩ) and 76.2 KΩcm^2 (R_0=107 MΩ) for sample A and sample B. Some measured data were listed in Table 5. Results showed that those detectors with n-on-p configuration exhibited better performance than those of p-on-n configuration. The dark current decreased more than one order of magnitude at room temperature for the detectors

with similar composition and doping level, which were mainly owing to the better quality of the absorption layer because of the heavy Be doped InAlAs graded buffer layer.
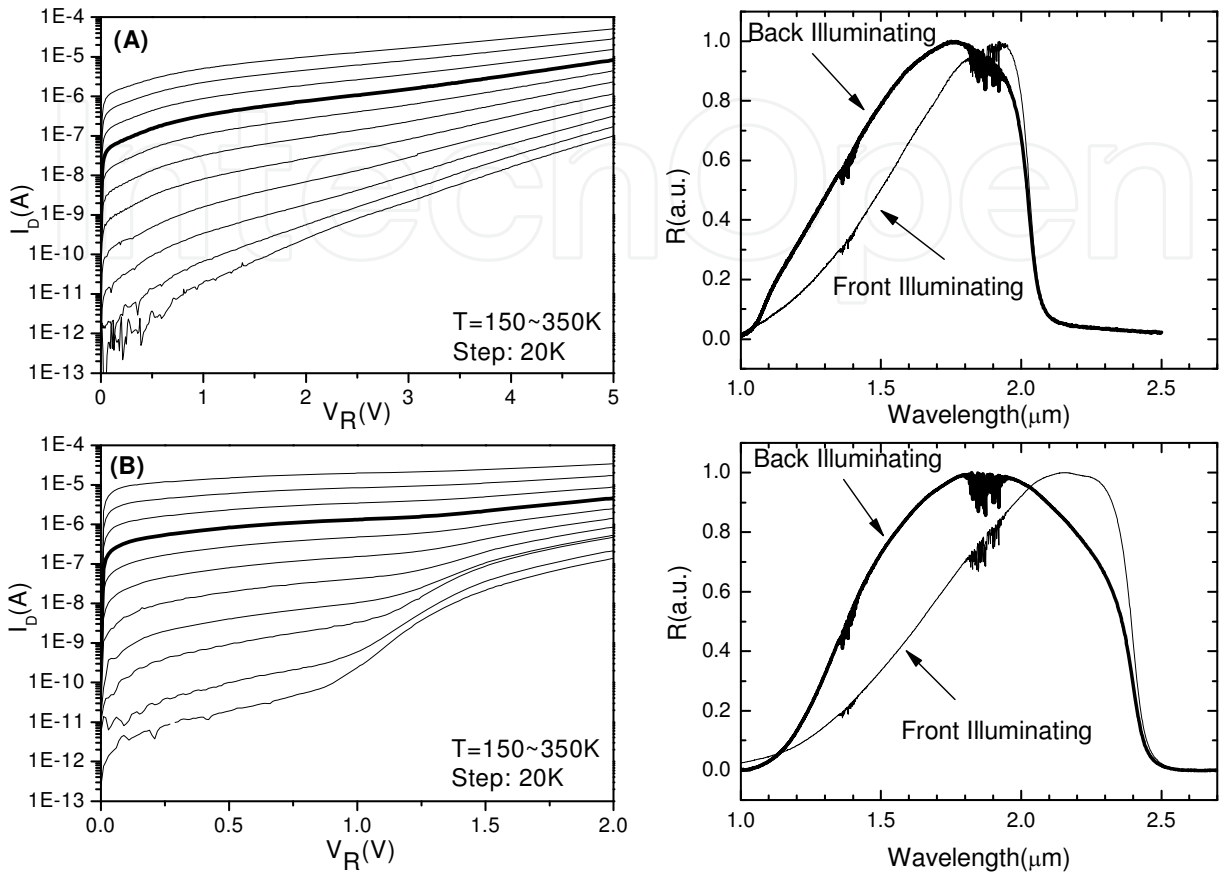

Fig. 17. Measured I-V (left) and room temperature response spectra (right) of the sample A (cutoff at 2.0 μm) and Sample B (cutoff at 2.4 μm) photodiodes.

$\Phi=300\mu m$ $N_D\sim3E16cm^{-3}$	Temp. (K)	I_D (nA) $V_R=10mV$	R_0A (Ωcm^2)	$D^*_{\lambda p}(R_0A)$ (cmHz$^{1/2}$/W) Back Illumn.	$D^*_{\lambda p}(R_0A)$ (cmHz$^{1/2}$/W) Front Illumn.
Sample A	290	11.3	760	1.534E11 ($\lambda p=1.75\mu m$)	1.700E11 ($\lambda p=1.94\mu m$)
	210	0.0307	250K	3.17E12 ($\lambda p=1.7\mu m$)	3.53E12 ($\lambda p=1.89\mu m$)
Sample B	290	75.1	104	5.933E10 ($\lambda p=1.83\mu m$)	7.132E10 ($\lambda p=2.2\mu m$)
	210	0.102	76.2K	1.80E12 ($\lambda p=1.75\mu m$)	2.19E12 ($\lambda p=2.12\mu m$)

Table 4. Measured dark current I_D and zero bias resistance area products R_0A data of the photodiodes at 290K and 210K. The detectivity at peak wavelength $D^*_{\lambda p}$ were calculated from the R_0A data (suppose external quantum efficiency $\eta=0.5$)
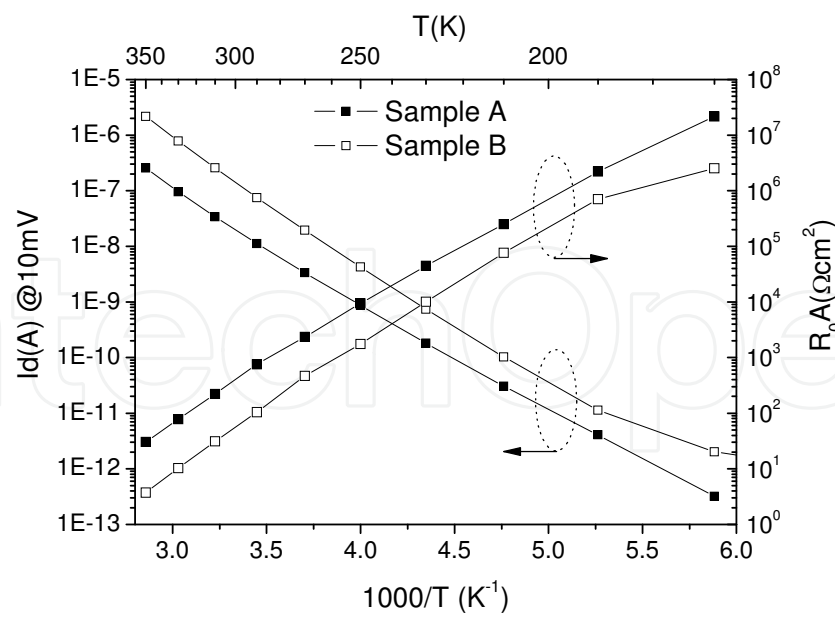
Fig. 18. Arrhenius plots of the dark current versus reciprocal temperature of the sample A (cutoff at 2.0 μm) and Sample B (cutoff at 2.4 μm) photodiodes at reverse bias voltage of 10mV. The zero bias resistance area products R_0A of the photodiodes were also plotted.

	Sample A		Sample B	
	Front Illumination	Back Illumination	Front Illumination	Back Illumination
Signal(mV) @10^{-6}A/V	10.8	4.32	27.5	10.3
Noise(μV) @10^{-8}A/V	220	220	540	540
S/N	4909	1963	5092	1907
G-Factor	27.27	25.59	13.07	13.19
$R_{\lambda p}$ (A/W)	0.65721	0.24618	0.79204	0.30205
$D^*_{\lambda p}$ (cmHz$^{1/2}$/W)	1.31E11	4.91E10	6.50E10	2.46E10

Table 5. Measured black body response of the $\Phi=500\mu m$ detectors at room temperature (~295K) using 900K black body source under front or back illumination. The detectivity at peak wavelength $D^*_{\lambda p}$ and current responsibility $R_{\lambda p}$ from the signal/noise ratio S/N and spectra G-Factor were also listed.

To evaluate the performance of the detector more directly, the black-body response measurements were performed at room temperature (~295 K) with a 900K black-body source. From the measured signal/noise ratio S/N and calculated G-factor from the response spectra, the peak detectivity $D^*_{\lambda p}$(BB) were calculated as listed in Table 5. Notice that for front illumination the $D^*_{\lambda p}$(BB) in consists with the calculated $D^*_{\lambda p}$(R_0A) quite well, whereas for back illumination the $D^*_{\lambda p}$(BB) is only about half of the $D^*_{\lambda p}$(R_0A), the signal was weaker but noise keeps unchanged. This was mainly because of the free carrier absorption of the P$^+$ InP substrate and diffuse reflection caused by imperfectness of the back side polishing. Therefore for back illumination the S. I. InP substrate should be used and backside polishing becomes important. The peak responsibilities R_λ of the detectors from the black body measurements were 0.657 A/W and 0.792 A/W for sample A and sample B respectively at front illumination condition, corresponding to an external quantum

efficiency of about 42% and 45%. For those detectors without AR coating this quantum efficiency is moderate.

5. Conclusion

In conclusion, benefited from the developments of InP based optoelectronic devices, wavelength extending $In_xGa_{1-x}As$ (x>0.53) photodetectors have been a remarkable candidate in SWIR band especially for the applications at higher operation temperatures and robust circumstances. For growing this lattice mismatched ternary thick layer on InP substrate the buffer layer is ineluctable. Though $In_xGa_{1-x}As$ itself could be used as graded buffer material (Zhang et al., 2006a), whereas the ternary $In_xAl_{1-x}As$(x>0.52), which is a compatible mate of $In_xGa_{1-x}As$ in MBE, is an excellent option especially for its wider bandgap needful to both performances and utilization of concern (Zhang et al., 2008b). Based on this advisement a convenient and reliable growth procedure with excellent feasibility has been developed for GSMBE (Zhang et al., 2008a), using this procedure a series of devices with anticipant performances have been demonstrated. Our efforts show that in front illumination conditions the $In_yAl_{1-y}As/In_yGa_{1-y}As/In_xAl_{1-x}As$ heterostructure device with p-on-n configuration is an outstanding choice, whereas for back illumination using n-on-p configuration becomes advisable (Zhang et al., 2009a). Our attempt also show that for this PDs the cutoff wavelength at room temperature could be extended to about 3 µm, at this wavelength the performances of this PDs are still competitive for certain applications at higher operation temperatures (Li et al., 2010).

6. References

Afrailov M. A. (2010). Photoelectrical characteristics of the InAsSbP based uncooled photodiodes for the spectral range 1.6-3.5 µm. *Infrared Physics & Technology,* 53(1), 29-32, ISSN: 1350-4495

Bhagwat V; Xiao Ye-gao; Bhat I et al. (2006). Analysis of leakage currents in MOCVD grown GaInAsSb based photodetectors operating at 2 µm. *J. Electronic Materials,* 35(8), 1613-1617, ISSN: 0361-5235

Chyi J I; Shieh J L; Pan J W et al. (1996). Material properties of compositional graded $In_xGa_{1-x}As$ and $In_xAl_{1-x}As$ epilayers grown on GaAs substrates. *J. Appl. Phys.* 79(11), 8367-8370, ISSN: 0021-8979

di Forte-Poisson M.A; Brylinski C; di Persio J et al. (1992). GaInAs/InAsP/InP photodiode for the 1.6 to 2.4 µm spectral region grown by low pressure MOCVD, *J. Crystal Growth,* 124(1-4), 782-791, ISSN: 0022-0248

Fewster P F, (1993). X-ray diffraction from low-dimensional structures. *Semicon. Sci. Technol.* 8(11), 1915-1934, ISSN: 0268-1242

Gu Yi; Li Cheng; Wang Kei et al. (2010). Wavelength extended InGaAs/InP photodetector structures with lattice mismatch up to 2.6%. *J. Infrared Millim. Waves,* 29(4), 81-86, ISSN: 1001-9014

Hao Guo-qiang; Zhang Yong-gang; Gu Yi et al. (2006). Performance analysis of extended wavelength InGaAs photovoltaic detectors grown with gas source MBE. *J. Infrared Millim. Waves*, 25(4), 241-245, ISSN: 1001-9014
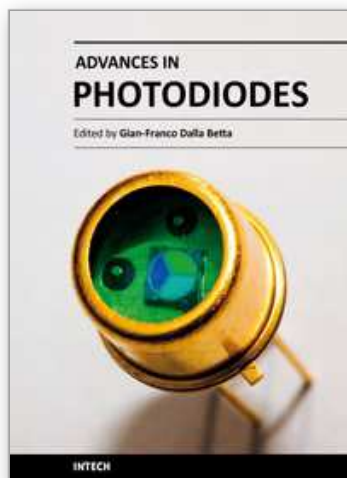
Hondt M.D; Moerman I; Daele P.V et al. (1998) Dark current optimization for MOVPE grown 2.5 μm wavelength InGaAs photodetectors, *Electron. Lett.*, 34(9), 910-912, ISSN: 0013-5194

Hoogeveen R.W.M; van der A R. J; Goede A.P.H et al. (2001). Extended wavelength InGaAs infrared (1.0-2.4 μm) detector arrays on SCIAMACHY for space-based spectrometer of the Earth atmosphere. *Infrared Phys. & Tech.* 42(1),1-16, ISSN: 1350-4495

Lee D; Park M S; Tang Z et al. (2007). Characterization of metamorphic InAlAs/GaAs buffer layers using reciprocal space mapping. *J. Appl. Phys.* 101(6), 063523(8pp), ISSN: 0021-8979

Li Ai-zhen, Zhong Jin-quan, Zheng Yan-lan et al. (1995). Molecular beam epitaxial growth, characterization and performance of high-detectivity InGaAsSb/GaSb PIN detectors operating at 2.0 to 2.6 μm. *J. Crystal Growth,* 150(2), 1375-1378 , ISSN: 0022-0248

Li Cheng; Zhang Yong-gang; Wang Kai et al. (2010). Distinction investigation of InGaAs photodetectors cutoff at 2.9 μm. *Infrared Physics & Technology*, 53(3), 173-176, ISSN: 1350-4495

Liang Bang-li; Chen Dian-yong; Wang Bo et al. (2010). Analysis, optimization and design of 2-2.8μm stacked multiple-junction PIN GaInAsSb/GaSb photodetectors for future O/E interconnections. *IEEE Trans. on Electron Devices,* 57(2), 361-367, ISSN: 0018-9383

Makita K; Torikai T; Ishihara H et al. (1988). GaInAs/InAsP pin photodiode for long wavelength region (λ>2μm) grown by hydride vapor phase epitaxy. *Electron. Lett.*, 24(7), 379-380, ISSN: 0013-5194

Moseley A. J; Scott M. D; Moore A. H et al. (1986). High-efficiency, low-leakage MOCVD grown GaInAs/AlInAs heterojunction photodiodes for detection to 2.4μm. *Electron. Lett.*, 22(22), 1206-1207, ISSN: 0013-5194

Piotrowski T. T; Piotrowska A; Kaminska E et al. (2001). Design and fabrication of GaSb/InGaAsSb/ AlGaAsSb mid-IR photodetectors. *Proc. SPIE*, 4413, 339, ISBN: 0-8194-4116-3

Quitoriano N J & Fitzgerald E A (2007). Relaxed, high-quality InP on GaAs by using InGaAs and InGaP graded buffers to avoid phase separation. *J. Appl. Phys.* 102(3), 033511(17pp), ISSN: 0021-8979

Rothman L. S; Jacquemart D; Barbe A et al. (2005) The HITRAN 2004 molecular spectroscopic database. *J. Quantitative Spectroscopy & Radiative Transfer*, 96(2), 139-204, ISSN: 0022-4073

Tersoff J. (1993). Dislocations and strain relief in compositionally graded layers. *Appl. Phys. Lett.* 62(7), 693-695, ISSN: 0003-6951

Tian Zhao-bing; Gu Yi & Zhang Yong-gang. (2008a). Quantum efficiency optimization of InP based In$_{0.53}$Ga$_{0.47}$As photodetectors. *J. Infrared Millim. Waves,* 27(2), 81-85, ISSN: 1001-9014

Tian Zhao-bing; Gu Yi; Wang Kai et al. (2008b). Gas source MBE grown metamorphic InGaAs photodetectors using InAlAs buffer and cap layers with cou-off wavelength up to 2.7 μm. *Chin. Phys. Lett.*, 25(6), 2292-2295, ISSN: 0256-307X

Tian Zhao-bing; Gu Yi; Zhang Xiao-Jun et al. (2008c). Quantum efficiency optimization of wavelength extended InGaAs photodetectors" *Chin. J. Semicon. Optoelectronics,* 29(6), 851-854, ISSN: 1001-5868 (in Chinese)

Uchida Y; Kakibayashi H; Goto S. (1993) Electrical and structural properties of dislocations confined in a InGaAs/GaAs heterostructure. *J. Appl. Phys.* 74(11), 6720-6725, ISSN: 0021-8979

Wada M & Hosomatsu H (1993). Wide wavelength and low dark current lattice-mismatched InGaAs/InAsP photodiodes grown by metalorganic vapour-phase epitaxy. *Appl. Phys. Lett.* 64(10), 1265-1267, ISSN: 0003-6951

Wang Kai; Zhang Yong-gang; Gu Yi et al. (2009). Improving the performance of extended wavelength InGaAs photodetectors by using digital graded heterointerface superlattice. *J. Infrared Millim. Waves,* 28(6), 405-409, ISSN: 1001-9014 (in Chinese)

Wel P J; Nijenhuis J; Eck E R H et al. (1992). High-spatial-resolution photoluminescence studies on misfit dislocations in lattice-mismatched III-V heterostructures. *Semicon. Sci. Technol.* 7(1A), A63-A70, ISSN: 0268-1242

Zhang Ke-feng; Tang Heng-jing; Wu Xiao-li et al. (2007a). Performance analysis of 256 element linear 2.4 μm InGaAs photovoltaic detector arrays. *Proc. SPIE,* 6835, 683506, ISBN: 9780819470102

Zhang Yong-gang; Zhou Ping; Chen Hui-ying et al. (1990). LPE growth of InAsPSb on InAs: melt composition, lattice mismatch and surface morphology. *Chin. J. Rare Metals,* 9(1), 48-51, ISSN: 1001-0521

Zhang Yong-gang; Zhou Ping; Shan Hong-kun et al. (1992). InAsPSb/InAs mid-infrared photodetectors. *Chin. J. Semiconductors,* 13(10), 623-628, ISSN: 0253-4177 (in Chinese)

Zhang Yong-gang; Hao Guo-qiang; Gu Yi et al. (2005). 1.9 μm InGaAs PIN Photodetectors Grown by Gas Source MBE. *Chin. Phys. Lett.,* 22(1), 250-253, ISSN: 0256-307X

Zhang Yong-gang; Gu Yi, Zhu Cheng et al. (2006a). Gas source MBE grown wavelength extended 2.2 and 2.5 μm InGaAs PIN photodetectors. *Infrared Physics & Technology,* 47(3), 257-262, ISSN: 1350-4495

Zhang Yong-gang; Gu Yi, ZHU Cheng et al. (2006b). Fabrication of short wavelength infrared InGaAs/InP photovoltaic detector series. *J. Infrared Millim. Waves,* 25(1), 6-9, ISSN: 1001-9014   (in Chinese)

Zhang Yong-gang; Zhang Xiao-jun; Zhu Xiang-rong et al. (2007b). Tunable diode laser absorption spectroscopy detection of N_2O at 2.1 μm using antimonide laser and InGaAs photodiode. *Chin. Phys. Lett.,* 24(8), 2301-2303, ISSN: 0256-307X

Zhang Yong-gang; Gu Yi; Tian Zhao-bing et al. (2008a). Wavelength extended 2.4 μm heterojunction InGaAs photodiodes with InAlAs cap and linearly graded buffer layers suitable for both front and back illuminations. *Infrared Physics & Technology,* 51(4), 316-321, ISSN: 1350-4495

Zhang Yong-gang; Gu Yi; Wang Kai et al. (2008b). Properties of gas source molecular beam epitaxy grown wavelength extended InGaAs photodetector structures on linear graded InAlAs buffer. *Semicon. Sci. Technol.* 23(12), 125029(7pp), ISSN: 0268-1242

Zhang Yong-gang; Gu Yi; Zhang Xiao-jun et al. (2008c). Gas sensor using a robust approach under time multiplexing scheme with a twin laser chip for absorption and reference" *Chin. Phys. Lett.,* 25(9), 3246-3249, ISSN: 0256-307X

Zhang Yong-gang; Gu Yi; Tian Zhao-bing et al. (2009a). Wavelength extended InGaAs/InAlAs/InP photodetectors using n-on-p configuration optimized for back illumination. *Infrared Physics & Technology,* 52(1), 52-56, ISSN: 1350-4495

Zhang Yong-gang; Gu Yi; Tian Zhao-bing et al. (2009b). Performance of gas source MBE grown wavelength extended InGaAs photodetectors with different buffer structures. *J. Crystal Growth,* 311(7), 1881-1884, ISSN: 0022-0248

Zimmermann L; John J; Degroote S et al. (2003). Extended wavelength InGaAs on GaAs using InAlAs buffer for back-side-illuminated short-wave infrared detectors. *Appl. Phys. Lett.* 82(17), 2838-2840, ISSN: 0003-6951

Advances in Photodiodes
Edited by Prof. Gian Franco Dalla Betta

ISBN 978-953-307-163-3

Hard cover, 466 pages

Publisher InTech

Published online 22, March, 2011

Published in print edition March, 2011

Photodiodes, the simplest but most versatile optoelectronic devices, are currently used in a variety of applications, including vision systems, optical interconnects, optical storage systems, photometry, particle physics, medical imaging, etc. Advances in Photodiodes addresses the state-of-the-art, latest developments and new trends in the field, covering theoretical aspects, design and simulation issues, processing techniques, experimental results, and applications. Written by internationally renowned experts, with contributions from universities, research institutes and industries, the book is a valuable reference tool for students, scientists, engineers, and researchers.

How to reference

In order to correctly reference this scholarly work, feel free to copy and paste the following:

Yong-gang Zhang and Yi Gu (2011). Gas Source MBE Grown Wavelength Extending InGaAs Photodetectors, Advances in Photodiodes, Prof. Gian Franco Dalla Betta (Ed.), ISBN: 978-953-307-163-3, InTech, Available from: http://www.intechopen.com/books/advances-in-photodiodes/gas-source-mbe-grown-wavelength-extending-ingaas-photodetectors

INTECH
open science | open minds